DWARF GALAXY FORMATION WITH H₂-REGULATED STAR FORMATION

Michael Kuhlen[1], Mark R. Krumholz[2], Piero Madau[2], Britton D. Smith[3], and John Wise[4,5]
[1] Theoretical Astrophysics Center, University of California, Berkeley, CA 94720, USA; mqk@astro.berkeley.edu
[2] Department of Astronomy and Astrophysics, University of California, Santa Cruz, CA 95064, USA
[3] Department of Physics and Astronomy, Michigan State University, East Lansing, MI 48824, USA
[4] Department of Astrophysical Sciences, Princeton University, Peyton Hall, Ivy Lane, Princeton, NJ 08544, USA

ABSTRACT

We describe cosmological galaxy formation simulations with the adaptive mesh refinement code Enzo that incorporate a star formation prescription regulated by the local abundance of molecular hydrogen. We show that this H_2-regulated prescription leads to a suppression of star formation in low-mass halos ($M_h \lesssim 10^{10}\,M_\odot$) at $z > 4$, alleviating some of the dwarf galaxy problems faced by theoretical galaxy formation models. H_2 regulation modifies the efficiency of star formation of cold gas directly, rather than indirectly reducing the cold gas content with "supernova feedback." We determine the local H_2 abundance in our most refined grid cells (76 proper parsec in size at $z = 4$) by applying the model of Krumholz, McKee, & Tumlinson, which is based on idealized one-dimensional radiative transfer calculations of H_2 formation–dissociation balance in $\sim$100 pc atomic–molecular complexes. Our H_2-regulated simulations are able to reproduce the empirical (albeit lower z) Kennicutt–Schmidt relation, including the low Σ_{gas} cutoff due to the transition from atomic to molecular phase and the metallicity dependence thereof, without the use of an explicit density threshold in our star formation prescription. We compare the evolution of the luminosity function, stellar mass density, and star formation rate density from our simulations to recent observational determinations of the same at $z = 4$–8 and find reasonable agreement between the two.

Key words: cosmology: theory – galaxies: dwarf – galaxies: formation – galaxies: halos – methods: numerical

Online-only material: color figures

1. INTRODUCTION

The ΛCDM paradigm of cosmological structure formation (White & Rees 1978; Blumenthal et al. 1984) has been tremendously successful at explaining the large-scale, statistical features of the distribution of matter in our universe (Springel et al. 2006). At the same time, it is also very clear that the mapping from dark matter halos to their baryonic components, to the properties of galaxies embedded within the halos, is far from straightforward and currently poorly understood. One prominent example of this lack of understanding is the fact that the cosmic mass-to-light relation is neither constant nor monotonic and instead exhibits a minimum at a galaxy mass of $10^{12}\,M_\odot$ (e.g., Conroy & Wechsler 2009). Evidently, some unknown processes are inhibiting efficient star formation (SF) on both larger and smaller mass scales.

The focus of this paper is on the low-mass end, the dwarf galaxies. There are (at least) two dwarf galaxy problems, which may or may not have the same explanation. The first of these is the well-known "Missing Satellites Problem" (Kauffmann et al. 1993; Klypin et al. 1999; Moore et al. 1999), which refers to the discrepancy between the relatively small number of satellite galaxies known to be orbiting the Milky Way and M31 ($\sim$20 around each) and the vastly larger number of dark matter subhalo satellites predicted from dark-matter-only cosmological numerical simulations ($\gtrsim 10^5$ in the latest simulations; Diemand et al. 2008; Stadel et al. 2009; Springel et al. 2008). Photoheating from the meta-galactic UV background will prevent gas from collapsing and forming stars in all but the most massive subhalos (Efstathiou 1992; Kauffmann et al. 1993; Bullock et al. 2000), but even so the number of dark matter subhalos that

should be able to host a luminous component, either because they collapsed prior to reionization or because they reached a sufficiently large mass thereafter, exceeds the current census of dwarf satellite galaxies by at least one order of magnitude (Madau et al. 2008). The interpretation of this discrepancy is further complicated by interactions with the host galaxy. Ram pressure stripping (Mayer et al. 2006), as well as resonant (D'Onghia et al. 2009) and tidal interactions (Gnedin et al. 1999) with the host's dark matter halo or stellar disk, could modify the abundance and properties of galactic satellite galaxies.

The second dwarf galaxy problem occurs in the field and is exemplified by the apparent inability of virtually all theoretical models of galaxy formation to match the abundance of low stellar mass galaxies at $z > 0$. Semi-analytic galaxy formation models (SAMs), for example, are able to match the observed stellar mass function in the local universe ($z = 0$) by judiciously tuning their active galactic nuclei, photoionization, and supernova feedback parameters, but these same models predict an abundance of $M_\star < 10^{10}\,M_\odot$ galaxies at higher redshifts that exceeds the observational constraints by an order of magnitude (Fontanot et al. 2009; Marchesini et al. 2009; Cirasuolo et al. 2010). Hydrodynamic galaxy formation simulations face similar problems (Nagamine et al. 2006; Cen & Ostriker 2006; Choi & Nagamine 2012). A closely related problem is the inability of numerical simulations and SAMs to match the low values of the stellar mass fraction and its strongly decreasing trend with halo mass, as inferred from observations and semi-empirical approaches (Guo et al. 2010; Avila-Reese et al. 2011).

Besides UV photoheating, stellar feedback, in the form of energy or momentum injection from supernovae explosions (Dekel & Silk 1986; Efstathiou 2000), stellar winds (Norman & Silk 1980; McKee 1989), or radiation pressure (Krumholz & Matzner 2009; Murray et al. 2010; Hopkins et al. 2011),

is commonly invoked to explain the reduction in SF efficiency in low-mass halos. In SAMs (Cole et al. 2000; Benson et al. 2003; Somerville et al. 2008; Wang et al. 2008) this type of feedback is typically modeled as a reduction of the cold gas reservoir available for SF, with an efficiency proportional to some power law of the galactic disk circular velocity.

In direct cosmological numerical simulations, stellar feedback remains subgrid physics even for today's state-of-the-art computational efforts. Cosmological zoom-in simulations of individual galaxies have reached tens of parsec resolution (Gnedin et al. 2009; Ceverino & Klypin 2009; Governato et al. 2010; Agertz et al. 2011; Faucher-Giguère & Kereš 2011; Guedes et al. 2011), but full-box global simulations are at least one order of magnitude behind (Ocvirk et al. 2008; Schaye et al. 2010; Oppenheimer et al. 2010; Choi & Nagamine 2012; Faucher-Giguère et al. 2011). Neither approach is able to resolve the $\lesssim$parsec scales on which stellar feedback actually operates in nature. Instead, simulators have turned to feedback prescriptions that are meant to capture the cumulative effect of supernova explosions on scales that are computationally accessible. A wide variety of such subgrid physics prescriptions have been implemented, ranging from a simple injection of thermal energy at the location of newly created star particles (Cen & Ostriker 1993), often with radiative cooling artificially turned off for some time to prevent the newly added energy from rapidly radiating away (Thacker & Couchman 2000; Stinson et al. 2006), to attempts at keeping track of separate cold and hot phases of the subgrid interstellar medium (ISM; Yepes et al. 1997; Gnedin 1998; Springel & Hernquist 2003), to direct kinetic feedback, in which momentum kicks are applied to surrounding gas particles (Springel & Hernquist 2003; Oppenheimer & Davé 2006; Schaye et al. 2010; Genel et al. 2012), which are subsequently temporarily decoupled from hydrodynamic forces (except in Schaye et al. 2010) in order to allow them to escape the star-forming region.

Although improvements in the stellar feedback treatment have indeed enabled progress in galaxy formation simulations, for example, the production of quasi-realistic disk galaxies from cosmological initial conditions (Governato et al. 2010; Agertz et al. 2011; Guedes et al. 2011; Avila-Reese et al. 2011; Piontek & Steinmetz 2011; Brook et al. 2012), the results depend sensitively on the details of the feedback implementations (Sales et al. 2010), which themselves are often based on ad hoc assumptions. Furthermore, many problems are not completely solved by stellar feedback as it is currently implemented. The inability of simulations and SAMs, even those including supernova feedback prescriptions, to match the observed high-redshift stellar mass functions and star formation rates (SFRs) is one example (Cirasuolo et al. 2010; Choi & Nagamine 2012). Another is the challenge of suppressing the stellar mass content of low-mass halos while simultaneously matching the observed mass–metallicity relation in Milky Way dwarf satellites (Font et al. 2011).

Important physical processes associated with SF are not captured by current models, and it is time to revisit the dwarf galaxy problems in light of new understanding of how SF actually occurs in the ISM of local galaxies. One promising direction is an improved treatment of the chemistry and thermodynamics of the interstellar gas that is actually forming stars. In particular, spatially resolved observations of local galaxies have revealed that SF correlates much more tightly with the density of *molecular* gas than total gas density (Wong & Blitz 2002; Kennicutt et al. 2007; Leroy et al. 2008; Bigiel et al. 2008). Even though

the primary cooling agents are lines of CO or C II (depending on the chemical state of the carbon), molecular hydrogen (H_2) is expected to be a good tracer of SF, even at low metallicities (Krumholz et al. 2011).

This motivates an SF prescription that differentiates between the chemical phases of the gas, in which the formation of star particles is tied to the local abundance of H_2, as opposed to the total gas density, as is more commonly done in numerical simulations. Indeed, some SAMs have begun to explore this direction (Fu et al. 2010; del P. Lagos et al. 2011; Krumholz & Dekel 2011), and several numerical simulations including H_2 physics have been published (Robertson & Kravtsov 2008; Gnedin et al. 2009; Feldmann et al. 2011). Until now these simulations focused only on individual galaxies, either in isolated disks or in cosmological zoom-in simulations. In this work we investigate for the first time the effect of an H_2-regulated SF prescription in full-box cosmological simulations, with an eye toward the statistical distribution of SF efficiency in dwarf galaxies.

Following the non-equilibrium H_2 chemistry in a realistic and self-consistent manner, including formation on dust grains and the radiative transfer of ionizing and dissociating radiation, is complicated and expensive to implement in numerical galaxy formation simulations (Gnedin et al. 2009). Fortunately, analytical one-dimensional (1D) radiative transfer calculations assuming H_2 formation–dissociation balance (Krumholz et al. 2008, 2009; McKee & Krumholz 2010) have shown that the H_2 abundance is determined to a good approximation (Krumholz & Gnedin 2011) by the H I column density and metallicity of gas on $\sim$100 pc scales. As these scales are directly accessible to us, we can bypass much of the computational difficulty associated with proper H_2 chemistry by implementing the Krumholz et al. (2009) results in our cosmological simulations. Even so, our use of cosmological adaptive mesh refinement (AMR) prevents our simulations from progressing much past $z \sim 4$ at an acceptable computational expense. Yet it is precisely in the early universe, at low but non-zero metallicities, that the metallicity dependence of the H I to H_2 transition will be most important, and its effect on SF greatest. Thanks to extensive multi-wavelength surveys (e.g., the Great Observatories Origins Deep Survey; Giavalisco et al. 2004) and deep follow-up observations with the *Hubble Space Telescope* (*HST*) and *Spitzer Space Telescope* (e.g., Stark et al. 2009; Bouwens et al. 2011; González et al. 2011; Labbé et al. 2010a), we are able to make contact with observational constraints on the cosmic stellar mass and SF density even at these high redshifts.

The main driver of this work, then, is to investigate to what degree a proper accounting of the H_2 abundance in star-forming gas can take the role that is traditionally assigned to supernova feedback, namely, a reduction of the SF efficiency in low-mass dark matter halos (see also Gnedin et al. 2009; Gnedin & Kravtsov 2010, hereafter G09; GK10). This paper is organized as follows. In Section 2 we describe our numerical approach and the details of our H_2-regulated SF prescription. We present the results of our work in Sections 3–5. We first show that our prescription reproduces many of the observational features of the SF scaling relations (Section 3). We then demonstrate that tying SF to the H_2 abundance indeed suppresses SF in low-mass halos, thereby alleviating the dwarf galaxy problems (Section 4). Finally, we present a direct comparison to recent observational determinations of the high-redshift evolution of the luminosity function (LF), stellar mass density (SMD), and SFR density (Section 5). We summarize and conclude in Section 6.

Table 1
Summary of the Simulations

Name	z_{final}	$\rho_{gas,SF}$	n_{thresh}	J_{LW}/J_{MW}	$[Z_{floor}]$	Comment
KT07	4.0	tot	$50\,cm^{-3}$	...	...	Krumholz & Tan (2007) SF law
KT07_low	6.0	tot	$5\,cm^{-3}$	...	...	Lower SF threshold
KT07_high	6.0	tot	$500\,cm^{-3}$	...	...	Higher SF threshold
KMT09	4.0	H_2	...	...	−3.0	Krumholz et al. (2009): two-phase equilibrium
KMT09_L8	6.0	H_2	...	...	−3.0	One additional refinement level (maxlevel = 8)
KMT09_FLW1	5.0	H_2	...	1	−3.0	KMT09 with uniform LW
KMT09_FLW10	5.0	H_2	...	10	−3.0	background of
KMT09_FLW100	5.0	H_2	...	100	−3.0	increasing
KMT09_FLW1000	5.0	H_2	...	1000	−3.0	intensity
KMT09_ZF4.0	6.0	H_2	...	...	−4.0	Lower Z_{floor}
KMT09_ZF2.5	6.0	H_2	...	...	−2.5	Higher Z_{floor}
KMT09_ZF2.0	6.0	H_2	...	...	−2.0	Even higher Z_{floor}
KMT09_ZFz10	6.0	H_2	...	...	−3.0	Z_{floor} at $z = 10$
KMT09_Sob	5.0	H_2	...	...	−3.0	Sobolev-like approximation of Σ
KMT09_SobL8	6.0	H_2	...	...	−3.0	KMT09_Sob with maxlevel = 8

Notes. All simulations have the same box size (12.5 Mpc) and were initialized at $z = 99$ with a WMAP7 cosmology: $\Omega_M = 0.265$, $\Omega_\Lambda = 0.735$, $\Omega_b = 0.045$, $h = 0.71$, $\sigma_8 = 0.801$, and $n_s = 0.963$. The number of dark matter particles is 256^3 ($m_p = 3.64 \times 10^6\,M_\odot$), and the root grid dimensions are also 256^3. We allow up to seven levels of adaptive mesh refinement, except in KMT09_L8, which has one additional level. $\rho_{gas,SF}$ indicates whether the SF prescription is tied to the total or H_2 gas density, n_{thresh} is the minimum density required for SF to occur (KT07 runs only), J_{LW}/J_{MW} is the intensity of the Lyman–Werner background normalized to the Milky Way's value (KMT09_FLW runs only), and $[Z_{floor}] \equiv \log_{10}(Z_{floor}/Z_\odot)$ is the initial seed metallicity applied at $z = 9$ in the KMT09 simulations.

2. SIMULATIONS

We have conducted cosmological AMR hydrodynamics simulations using Enzo ver. 2.0[6] to follow galaxy formation in the early ($z > 4$) universe. The computational domain covers a $(12.5\ Mpc)^3$ box with a root grid of 256^3 grid cells. The dark matter density field is resolved with 256^3 particles of mass $3.1 \times 10^6\,M_\odot$. The box has mean overdensity of zero, and no additional density fluctuation on the scale of the simulation box ("DC mode;" Gnedin et al. 2011) has been applied. AMR is allowed to occur throughout the entire domain for a maximum of seven levels of refinement, resulting in a maximum spatial resolution of $\Delta x_7 = 76.3 \times 5/(1 + z)$ proper parsec. Mesh refinement is triggered by a grid cell reaching either a dark matter mass equal to four times the mean root grid cell dark matter mass, or a baryonic mass equal to $8 \times 2^{-0.4l}$ times the mean root grid cell baryonic mass, where l is the grid level. The negative exponent in the baryonic refinement mass threshold implies a super-Lagrangian refinement criterion that results in more aggressive refinement at higher resolution. The simulations are initialized at $z_i = 99$ with the Eisenstein & Hu (1999) transfer function and cosmological parameters consistent with the *Wilkinson Microwave Anisotropy Probe* (*WMAP*) seven-year results (Komatsu et al. 2011): $\Omega_M = 0.265$, $\Omega_\Lambda = 0.735$, $\Omega_b h^2 = 0.02264$, $h = 0.71$, $n = 0.963$, and $\sigma_8 = 0.801$. The parameters of our suite of simulations are summarized in Table 1.

The equations of hydrodynamics are solved using Enzo's implementation of the piecewise parabolic method (Colella & Woodward 1984), a higher order accurate Godunov scheme. We utilize the recently added HLLC Riemann solver (Toro et al. 1994) with a fallback scheme to the more diffusive HLL solver for problematic cells, which greatly aids the simulations' stability. Enzo employs a dual-energy formalism (Bryan et al. 1995), solving for both the internal gas energy and total energy separately, to ensure accurate pressures and temperatures in hypersonic flows.

Our simulations include radiative cooling from both primordial- and metal-enriched gas, as well as photoheating from an optically thin, uniform meta-galactic UV background. The primordial gas cooling rates are calculated from the ionization states of hydrogen and helium, which are followed with a six-species (H, H^+, He, He^+, He^{++}, and e^-) non-equilibrium chemical network (Abel et al. 1997; Anninos et al. 1997), including collisional and photoionization/excitation rates. The metal cooling is determined from a five-dimensional table (independent variables: density, temperature, electron fraction, metallicity, and redshift) of heating and cooling rates precomputed with the Cloudy code (Ferland et al. 1998), as described in detail in Smith et al. (2008, 2011). For the UV background we used the updated version of the Haardt & Madau (2001) UV background model that ships with version 07.02.01 of Cloudy. This model includes the contributions of both quasars and galaxies in a redshift-dependent manner and is in reasonable agreement with a more recent calculation of the cosmic UV background (Faucher-Giguère et al. 2009).

As is commonly done in Eulerian hydrodynamic galaxy formation simulations (Machacek et al. 2001; Robertson & Kravtsov 2008; Agertz et al. 2009; Ceverino & Klypin 2009), we apply an artificial pressure support to cells that have reached the maximum refinement level. This is necessary in order to stabilize these cells against artificial fragmentation and is supposed to mimic the pressure support from turbulent motions below the simulation's resolution. In Enzo this support is implemented by increasing the internal gas energy up to some multiple of the value required to make the cell Jeans stable. We have set this factor equal to 10, meaning that the Jeans length of the highest resolution cells is artificially set to $\sqrt{10} \approx 3$ times the cell width.

2.1. Star Formation Prescriptions

The SF prescriptions we have implemented are all variations on the basic Schmidt law, whereby the local SFR in a grid cell

is proportional to its gas density divided by an SF timescale,

$$\dot{\rho}_{\rm SF} = \epsilon \, \frac{\rho_{\rm gas}}{t_\star}. \qquad (1)$$

In all of our simulations we set the SF timescale equal to the local free-fall time,

$$t_\star = t_{\rm ff} = \sqrt{\frac{3\pi}{32 \, G \, \rho_{\rm gas}}}, \qquad (2)$$

and fix the SF efficiency to $\epsilon = 0.01$, as motivated by Krumholz & Tan (2007), who showed that the local SF efficiency per free-fall time is low ($\epsilon_{\rm SF} \equiv \Sigma_{\rm SFR}/(\Sigma_{\rm gas} \, t_{\rm ff}) \approx 0.01$) and approximately constant over four orders of magnitude in density.

In Enzo's standard routines, SF is allowed to occur at every time step and in every grid cell that is not further refined. Provided that the cell fulfills all conditions for SF, a fraction of the cell's gas mass is converted into a star particle of mass $m_p = \epsilon \, \rho_{\rm gas} \, (\Delta x)^3 (\Delta t/t_\star)$. For highly refined cells with small time steps Δt, this commonly results in very large numbers of low-mass star particles, which can dramatically slow down the simulation's progress. Applying a mass threshold, below which a star particle is simply not created, is undesirable, since it can lead to a significant amount of "unfulfilled" SF, although this can be remedied with a stochastic SF criterion (e.g., Springel & Hernquist 2003 and see below).

To overcome these difficulties, we have modified Enzo's routines to allow SF to occur only *once per root grid time step* and only in cells at the *highest refinement level* (here $l = 7$), but with a star particle mass proportional to the root grid time step Δt_0 (see Kravtsov 2003), i.e.,

$$m_p = \epsilon \, \rho_{\rm gas} \, (\Delta x_7)^3 \, \frac{\Delta t_0}{t_\star}. \qquad (3)$$

Making m_p proportional to the root grid time step ($\Delta t_0 \gg \Delta t_7$) goes a long way toward overcoming the problem of large numbers of low-mass star particles. Nevertheless, we also enforce a minimum star particle mass of $m_{\rm min} = 10^4 \, M_\odot$, since even Δt_0 can occasionally become very small. Below this mass we implement a stochastic SF criterion as follows: if $m_p < m_{\rm min}$, we form a particle of mass equal to $m_{\rm min}$ if a randomly generated number is smaller than $(m_p/m_{\rm min})$.

We consider two distinct classes of SF prescriptions.

1. *Standard SFR (KT07)*: the SFR is proportional to the *total* gas density divided by the free-fall time, resulting in an SFR proportional to $\rho_{\rm h}^{3/2}$. We apply a density threshold below which SF is not allowed to occur and vary this threshold between values of 5, 50, and 500 cm^{-3}.

2. *H$_2$-regulated SFR (KMT09)*: the SFR is proportional to the *molecular hydrogen* density divided by the free-fall time determined from the total gas density, resulting in an SFR proportional to $f_{\rm H_2} \rho_{\rm h}^{3/2}$. The H$_2$ fraction, $f_{\rm H_2} = \rho_{\rm H_2}/\rho_{\rm h}$, is determined following Krumholz et al. (2009; more details in Section 2.2), and we consider both the two-phase equilibrium model and a range of models with different Lyman–Werner (LW) H$_2$-dissociating background intensities. No density threshold is applied.

The resolution of our simulations is not sufficient to resolve the formation sites of the first generation of stars, the so-called Population III. In order to capture the metal enrichment

resulting from the supernova explosions of this primordial stellar population, we instantaneously introduce a metallicity floor of $[Z_{\rm floor}] \equiv \log_{10}(Z_{\rm floor}/Z_\odot) = -3.0$ at $z = 9$, as motivated by recent high-resolution numerical simulations of the transition from Population III to Population II SF (Wise et al. 2012). This ensures the presence of a minimum amount of metals, which seed subsequent SF and further metal enrichment. We discuss the sensitivity of our results to the time and amplitude of this metallicity floor in Section 4.3.

2.2. Molecular Chemistry

To obtain the molecular hydrogen mass fraction $f_{\rm H_2} \equiv \rho_{\rm H_2}/\rho_{\rm h}$ in a given grid cell, we follow the analytical model developed in Krumholz et al. (2008, 2009) and McKee & Krumholz (2010). This model is based on a radiative transfer calculation of an idealized spherical giant atomic–molecular complex, subject to a uniform and isotropic LW radiation field. The H$_2$ abundance is calculated assuming formation–dissociation balance. The solution of this problem can conveniently be expressed in three lines:

$$f_{\rm H_2} \simeq 1 - \frac{3}{4} \frac{s}{1 + 0.25 \, s}, \qquad (4)$$

$$s = \frac{\ln(1 + 0.6\chi + 0.01\chi^2)}{0.6 \, \tau_c}, \qquad (5)$$

$$\chi = 71 \left(\frac{\sigma_{d,-21}}{\mathcal{R}_{-16.5}} \right) \frac{G_0'}{n_{\rm H,0}}, \qquad (6)$$

where τ_c is the dust optical depth of the cloud, $\sigma_{d,-21}$ is the dust cross section per H nucleus to 1000 Å radiation, normalized to a value of 10^{-21} cm^{-2}, $\mathcal{R}_{-16.5}$ is the rate coefficient for H$_2$ formation on dust grains, normalized to the Milky Way value of $10^{-16.5}$ cm^3 s^{-1} (Wolfire et al. 2008), G_0' is the ambient UV radiation field intensity, normalized to the Draine (1978) value for the Milky Way, and $n_{\rm H,0}$ is the volume density of H nuclei in units of cm^{-3}. Since both σ_d and $\mathcal{R}$ are linearly proportional to the dust abundance, their ratio is independent of the gas metallicity.

Krumholz et al. (2009) showed that a further simplification to the model can be made if the ISM is assumed to be in two-phase equilibrium between a cold neutral medium (CNM) and a warm neutral medium (WNM; Wolfire et al. 2003). The assumption of pressure balance between these two ISM components forces the minimum CNM density to be linearly proportional to the intensity of the LW radiation field, with only a weak dependence on metallicity:

$$n_{\rm min} \approx \frac{31}{1 + 3.1 \, (Z/Z_{\rm SN})^{0.365}} \, G_0', \qquad (7)$$

where $Z_{\rm SN}$ is the gas-phase metallicity in the solar neighborhood, and we set $Z_{\rm SN} = Z_\odot$ (Rodríguez & Delgado-Inglada 2011) and $Z_\odot = 0.0204$. Allowing for the typical CNM density to be somewhat higher than this minimum value, $n = \phi_{\rm CNM} \, n_{\rm min}$, we get

$$\chi = 2.3 \left(\frac{\sigma_{d,-21}}{\mathcal{R}_{-16.5}} \right) \frac{1 + 3.1 \, (Z/Z_{\rm SN})^{0.365}}{\phi_{\rm CNM}}, \qquad (8)$$

which renders $f_{\rm H_2}$ completely independent of the LW intensity. As in Krumholz & Gnedin (2011), we set $\phi_{\rm CNM} = 3$ and $(\sigma_{d,-21}/\mathcal{R}_{-16.5}) = 1$.

We have conducted one simulation with this two-phase equilibrium assumption (KMT09) and a range of simulations

without it, for which we instead specify a spatially uniform LW background intensity equal to 1, 10, 100, and 1000 times the present-day Milky Way value of 7.5×10^{-4} LW photons cm^{-3} (Draine 1978; KMT09_FLW1, . . . , KMT09_FLW1000). We directly apply these prescriptions to the highest resolution grid cells in our simulations, whose size ($\Delta x_7 = 54.5 \times 7/(1 + z)$ proper parsec) is comparable to the physical dimensions of giant atomic–molecular complexes (Blitz 1993). The dust optical depth is given by

$$\tau_c = \Sigma/\mu_H \, \sigma_d$$
$$\simeq 0.067 \left(\frac{Z}{Z_{SN}} \right) \left(\frac{\rho \, \Delta x_7}{1 \, M_\odot \, \text{pc}^{-2}} \right), \qquad (9)$$

where $\Sigma = \rho \, \Delta x_7$ is the cell's column density, $\mu_H = 2.3 \times 10^{-24}$ g is the mean mass per H nucleus, and we have set the dust cross section per H nucleus to be $\sigma_d = 10^{-21} \, (Z/Z_{SN})$ cm^2.

The use of Δx_7 in the calculation of Σ introduces an undesirable explicit resolution dependence in our algorithm, the effect of which we investigate in Sections 3.4 and 4.2. A Sobolev-like approximation, $\Sigma_{Sob} \equiv \rho \times (\rho/\nabla\rho)$ (e.g., G09; Krumholz & Gnedin 2011), would remove the explicit dependence of the algorithm on the width of the finest grid cells. As discussed in detail in the Appendix, we have conducted additional simulations using Σ_{Sob} in the KMT09 prescription, and these resulted in slightly lower column densities and reduced SF rates. At densities relevant for SF ($n > 5$ cm^{-3}), the differences between the two approximations of Σ are small, less than 20% in the median with a scatter of 0.26 dex, and well within the range of uncertainty of the parameters of the KMT09 model. The results presented in this paper were obtained with the simpler and computationally less expensive direct cell-based approximation using $\Sigma_{cell} \equiv \rho \Delta x_7$.

Regardless of how the surface density of atomic–molecular complexes is calculated, we should expect some degree of residual resolution dependence in our simulations, since we do not include the necessary stellar feedback physics (see below) that regulates the structure of molecular clouds and provides pressure support against further collapse. The artificial pressure support mentioned above, which we apply in order to avoid spurious fragmentation, is resolution dependent, and hence higher numerical resolution (through additional refinement levels) will always result in further collapse and higher densities in our simulations.

The KMT09 model has recently been tested against numerical simulations that self-consistently follow the formation and destruction of H$_2$ with a non-equilibrium chemical network including time-dependent and spatially inhomogeneous three-dimensional (3D) radiative transfer of UV and ionizing radiation (Krumholz & Gnedin 2011). The analytical model agrees extremely well with the numerical results whenever the metallicity is around 1% solar or greater. This agreement holds for both "fixed ISM" simulations in which the metallicity and radiation field are kept constant and cosmological simulations in which the metallicity and radiation field are computed self-consistently. At metallicities below 1% solar, the analytical model *overestimates* f_{H_2}. Note that for the runs without the two-phase equilibrium assumption, we follow Krumholz & Gnedin (2011) and apply a "clumping factor" of 30 to the H$_2$ formation rate (i.e., ($\sigma_{d,-21}/\mathcal{R}_{-16.5}$) = 1/30) to account for unresolved density inhomogeneities below our simulations' resolution limit. We do not use a clumping factor for the two-phase equilibrium model, because the two-phase model is in effect a direct estimate of the proper clumping factor. This physically motivated clumping model obviates the need for an ad hoc correction.

2.3. Feedback

Although we explore in this work to what degree an improved treatment of the ISM's chemical state can replace the need for stellar feedback in regulating SF, some form of feedback is necessary even in our simulations, if only to enrich the gas with metals that promote the formation of molecular hydrogen. For this purpose we employ a very simple feedback mechanism that is meant to simultaneously account for the mass, metals, and thermal energy deposited by winds from massive stars and core-collapse supernovae. The feedback is applied instantaneously at the time of formation of the star particle, is deposited into the $l = 7$ grid cell containing the particle, and consists of the following three components: (1) a fraction $\epsilon_m = 0.25$ of the star particle's mass is returned as gas, $\Delta m_{tot} = \epsilon_m \, m_p$; (2) the gas is enriched with a metal yield of $Y = 0.02$, $\Delta m_Z = \Delta m_{tot}(Y(1 - Z_p) + Z_p)$, where Z_p is the metallicity of the star particle and the two terms correspond to newly and previously enriched ejected material, respectively; (3) the thermal energy of the gas cell is increased by a fraction $\epsilon_{SN} = 10^{-5}$ of the rest-mass energy of the newly formed star particle, $\Delta E = \epsilon_{SN} \, m_p c^2$.

This feedback implementation is commonly applied in cosmological hydrodynamics simulations, but in fact it is known to be insufficiently strong. The problem with this instantaneous and localized feedback is that the thermal energy is applied to grid cells with very high gas density, in which the cooling time is very short. The injected energy is thus almost immediately lost to radiative cooling, and the feedback "fizzles out" (Katz 1992). We acknowledge the shortcoming of our current feedback implementation, but since we are focusing here on the global effects of different SF prescriptions, we defer attempts at improving the treatment of feedback to future work.

Finally, we caution that nothing in our implementation of molecular chemistry obviates the need to rely on a subgrid model of SF. Our model should be viewed in the same light as other subgrid models in wide use, e.g., the two-phase model of Springel & Hernquist (2003) or the blast wave model of Stinson et al. (2006). The main advantage of our new model is that it incorporates an explicit metallicity dependence, which both observations and theory appear to demand, as we discuss in more detail below.

2.4. Halo Population

We used the HOP halo finder (Eisenstein & Hut 1998) to identify gravitationally bound dark matter halos in our simulations. For every halo we determined the halo center (defined as the location of the highest dark matter density), the virial radius and corresponding mass (defined as the radius enclosing $\Delta_{vir} \approx$ times the background density (Bryan & Norman 1998)), and the amount of gas (total, H I, H II, H$_2$, He I, He II, and metals) contained within the halo.

Figure 1 shows the cumulative mass function of the simulations at $z = 4$, compared to the Sheth & Tormen (1999) fit. The agreement is remarkably good down to $M \approx 2 \times 10^9 \, M_\odot$, corresponding to halos with ~500 dark matter particles. At even lower mass numerical resolution effects lead to an artificial suppression in the number of halos. A finer root grid resolution and a more aggressive dark-matter-based refinement criterion would extend the mass function by another order of magnitude in mass
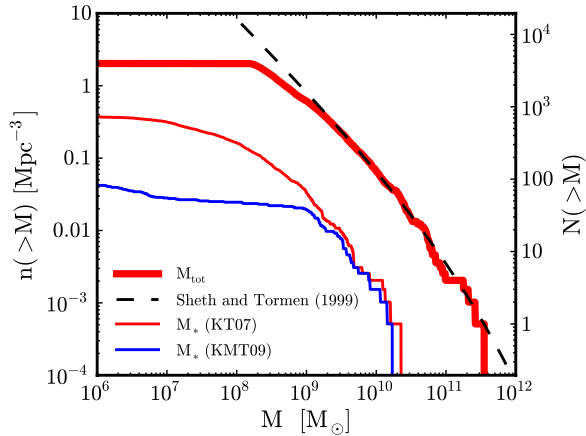
Figure 1. Cumulative mass function of halos in our simulations at $z = 4$. The thick line is for total mass (KT07 and KMT09 curves are almost indistinguishable, so we only show KT07), and the thin lines are for the stellar mass. The dashed line shows the Sheth & Tormen (1999) mass function fit. The right ordinate gives the total number of objects found in our $(12.5 \text{ Mpc})^3$ simulation volume.

(A color version of this figure is available in the online journal.)

(O'Shea et al. 2005). For our purposes, however, a resolution limit of $\sim 2 \times 10^9 \, M_\odot$ is sufficient, since halos with $M < 10^9 \, M_\odot$ lie below the UV suppression scale). Furthermore, as we show in Section 4, H_2-regulated SF leads to a suppression of stellar mass in halos with $M \lesssim 10^{10} \, M_\odot$. As a brief preview of this effect, we overplot in Figure 1 the cumulative *stellar* mass functions: the KMT09 simulation has far fewer low stellar mass ($M_\star < 10^9 \, M_\odot$) galaxies, which is a result of the suppression of SF in halos with $M \lesssim 10^{10} \, M_\odot$.

3. THE KENNICUTT–SCHMIDT LAW

A common test for a new numerical SF implementation is to compare the simulations to the observational Kennicutt–Schmidt (hereafter KS) relation, the empirical power law between the SFR surface density and total gas surface density: $\Sigma_{SFR} \propto \Sigma_{gas}^n$, with $n \approx 1.4$ (Kennicutt 1998; Daddi et al. 2010; Genzel et al. 2010).

In order to facilitate comparisons to observational data, we determine column densities by integrating through the density fields along the direction perpendicular to the stellar disk of the simulated galaxies. For Σ_{SFR} we integrate an SFR density defined as

$$\rho_{SFR} = \sum_{\text{age} < \tau_\star} \frac{m_\star}{\tau_\star \, (\Delta x)^3}, \qquad (10)$$

where Δx is the cell width, $m_\star$ is the star particle mass, and $\tau_\star = 10$ Myr is the SF averaging timescale, which roughly corresponds to observational SFR estimated from nebular emission lines ($H\alpha$, O III) or FIR continuum, but is a factor of 5–10 shorter than estimates based on FUV measurements (Kennicutt 1998; Feldmann et al. 2011). The sum in Equation (10) is over all star particles with age less than $\tau_\star$.

We calculate Σ_{gas}, Σ_{H_2}, Σ_{HI}, and Σ_{SFR} on a 1000×1000 pixel grid covering a 10×10 kpc region centered on each galaxy in a sample of 35 of the most massive galaxies in our simulations, chosen to cover a wide range in mean metallicity (see Section 3.2). We only considered galaxies in which the AMR reached the maximum level ($l = 7$). Visualizations of Σ_{SFR}, Σ_{gas}, Σ_{H_2}, and a density-weighted projection of metallicity are shown in Figure 2 for four representative massive galaxies in the KMT09 simulation at $z = 4$.

The observational KS relation, as reported for example by Daddi et al. (2010) and Genzel et al. (2010), has been established from a wide variety of data out to $z \gtrsim 3$, including spatially resolved local $z = 0$ spiral galaxies, infrared-selected starbursting galaxies and (U)LIRGs, BzK-selected galaxies at $z \approx 1.5$, "normal" star-forming galaxies at $z = 1$–2.3, and starbursting submillimeter galaxies (SMGs) at $z \approx 1$–3 (see Kennicutt 1998; Daddi et al. 2010; Genzel et al. 2010 for references). A reproduction of the observational relation from Daddi et al. (2010; their Figure 2) is shown in the left panel of Figure 3.

Our simulated galaxies are dwarf galaxies with stellar masses less than $10^{10} \, M_\odot$ at high redshift $z \geqslant 4$, and hence not directly comparable to any of these observational galaxy samples. Nevertheless, since SF is a local process, it makes sense to directly compare our simulated KS relation to the observations, as a test of how well our SF prescription is performing. The center and right panels of Figure 3 show this comparison for the KT07 and KMT09 simulations at $z = 4$. Since the 10 pc intrinsic resolution of our surface density maps is finer than in most spatially resolved studies to date (e.g., Bigiel et al. 2008; Bolatto et al. 2011), we downgrade the spatial resolution to 200 pc by spatially averaging with a 20 cell boxcar average. We explore the resolution dependence of our KS relations in Section 3.3. Only pixels with non-zero Σ_{SFR} are plotted. The solid line represents a sliding average of $\log_{10} \Sigma_{gas}$ in $\log_{10} \Sigma_{SFR}$ bins of width 0.5.

Both the amplitude and the slope of the relation are qualitatively in very good agreement with the observations. Such agreement has previously been reported (Kravtsov 2003; Gnedin & Kravtsov 2010, 2011; Feldmann et al. 2011), and we show it here merely to demonstrate that our new SF algorithm is valid and that the use of our H_2-regulated SF prescription does not destroy this agreement. We note that Kravtsov (2003) showed that even a *linear* local SF law, with a constant SF timescale $t_\star$ and a density threshold, can, when spatially averaged on $\lesssim$kpc scales, result in a super-linear surface density relation in agreement with the empirical KS law. Matching the observed KS law in cosmological simulations is thus not a good way to distinguish between different SF implementations.

Another cross-check with observational data is provided by the demonstration in Figure 4 that our simulated galaxies exhibit a similar relation between their SFR and total H_2 content as the galaxies in the study by Daddi et al. (2010). Our simulated relation has the same slope and lies in amplitude between what they refer to as the "sequence of starbursts" and the "sequence of disks." Note that a somewhat higher SFR at a given H_2 mass may be expected for lower metallicity systems, for which the transition to H_2 occurs at higher column densities.

3.1. Low Σ_{gas} SF Threshold

Both KT07 and KMT09 simulations exhibit a drop off in Σ_{SFR} at $\Sigma_{gas} \approx 50 \, M_\odot \text{ pc}^{-2}$. This feature is believed to correspond to saturation in the atomic hydrogen fraction, with gas becoming primarily molecular at higher surface densities (Bigiel et al. 2008). Since Σ_{SFR} appears to be almost independent of Σ_{HI} and instead correlates primarily with Σ_{H_2}, this H I saturation point is reflected in a kink toward lower SFR in the KS relation.

In the KT07 simulation, which does not account for the atomic-to-molecular hydrogen transition, this cutoff is reproduced by the density threshold imposed on the SF. In Figure 5 we show how the simulated KS relation depends on the value of this threshold. As expected, the relation extends to lower Σ_{gas}
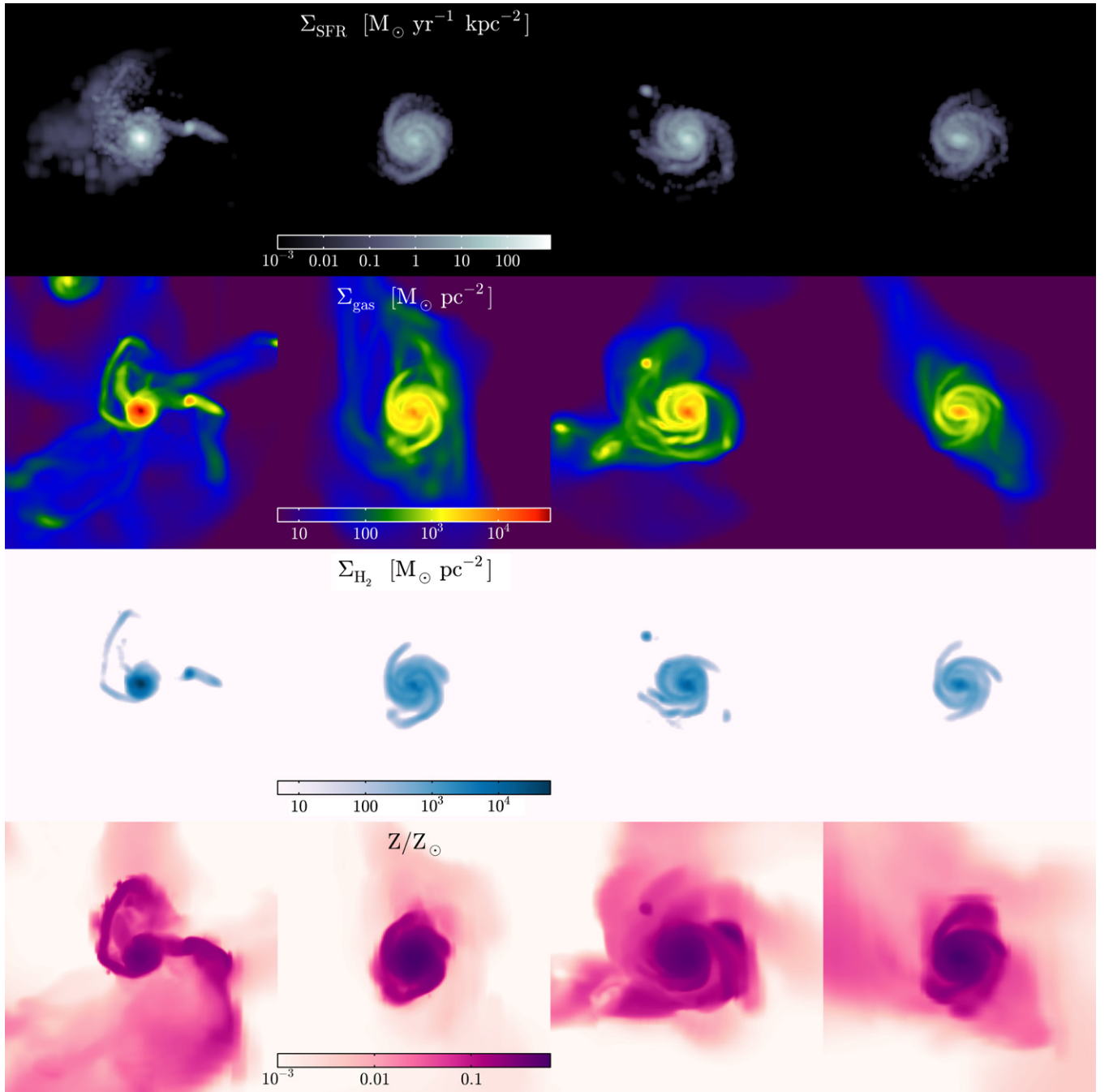
Figure 2. Surface density of SFR, total gas, H_2, and metallicity for four representative massive halos ($M_h = 2.5 \times 10^{11}$, 2.0×10^{11}, 1.6×10^{11}, $7.4 \times 10^{10}\,M_\odot$) in the KMT09 simulation at $z = 4$. The projections are calculated as line integrations perpendicular to the disk plane, for a 1000×1000 pixel grid covering a 10×10 kpc region centered on each galaxy.

(A color version of this figure is available in the online journal.)

for the lower threshold $n_{\rm thresh} = 5$ cm^{-3} case and steepens at a larger value of $\Sigma_{\rm gas} \approx 100\,M_\odot$ pc^{-2} when the threshold is higher, $n_{\rm thresh} = 500$ cm^{-3} (see also Colín et al. 2010). Once the SF is regulated by H_2, however, this turnover arises naturally: although the curve is noisier due to the smaller statistics, the relation appears to naturally steepen at $\Sigma_{\rm gas} \approx 50\,M_\odot$ pc^{-2}. This confirms the earlier results found by GK10 for a set of cosmological zoom-in galaxy formation simulations including non-equilibrium H_2 formation and radiative transfer.

Note that in the KMT09 KS relation (right panel of Figure 3) there are a few points with very low $\Sigma_{\rm gas}$ yet non-zero $\Sigma_{\rm SFR}$ and

a roughly corresponding number of points with high $\Sigma_{\rm gas}$ yet values of $\Sigma_{\rm SFR}$ significantly below the KS relation. These points arise from star particles having wandered out of the high-density cells in which they were born into a neighboring $l_{\rm avg}$ cell with much lower $\Sigma_{\rm gas}$. The degree to which this wandering causes a smearing in the KS relation depends on the spatial and temporal averaging scales employed in calculating $\Sigma_{\rm gas}$ and $\Sigma_{\rm SFR}$ and on the stars' velocity dispersion.

In local normal disk galaxies stellar velocity dispersions are typically only 5–10 km s^{-1}, preventing stars from wandering over more than a small fraction of the $\sim$kpc smoothing scale
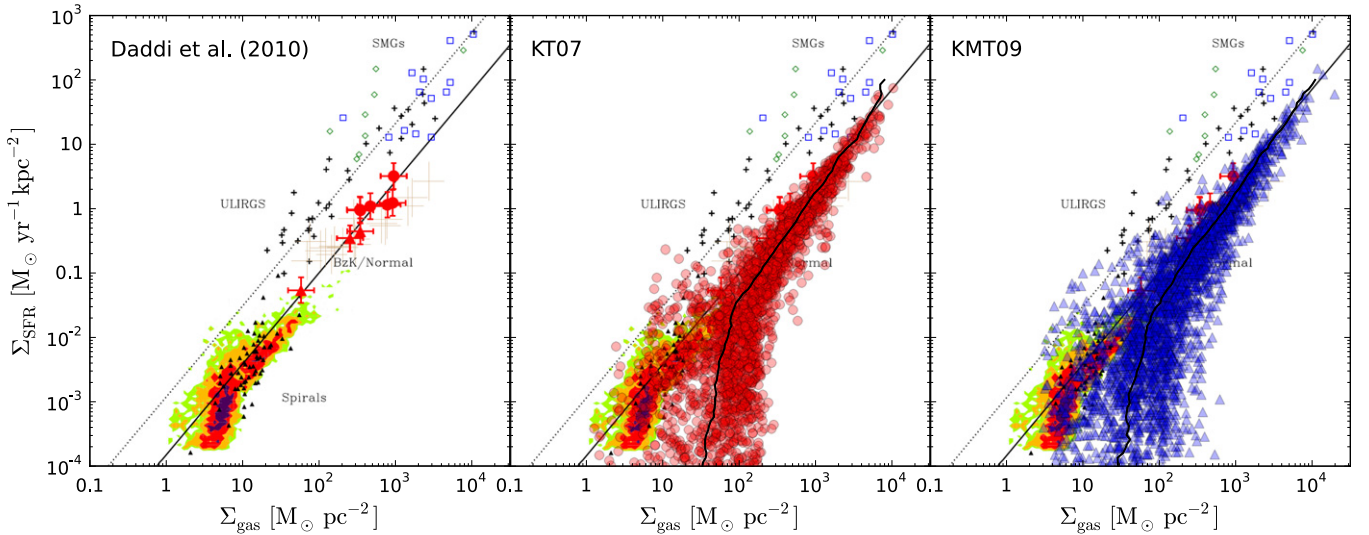
Figure 3. Comparison of the observational Kennicutt–Schmidt relation from Daddi et al. (2010) (left panel) to a standard SF simulation with SF density threshold of $n_{thresh} = 50$ cm^{-3} (middle), and an H$_2$-regulated SF simulation without any density threshold (right) at $z = 4$. In the simulations the surface densities have been determined from line integrations perpendicular to the galaxies' disk plane and have been smoothed to a resolution of 200 pc (see the text for more detail).

(A color version of this figure is available in the online journal.)
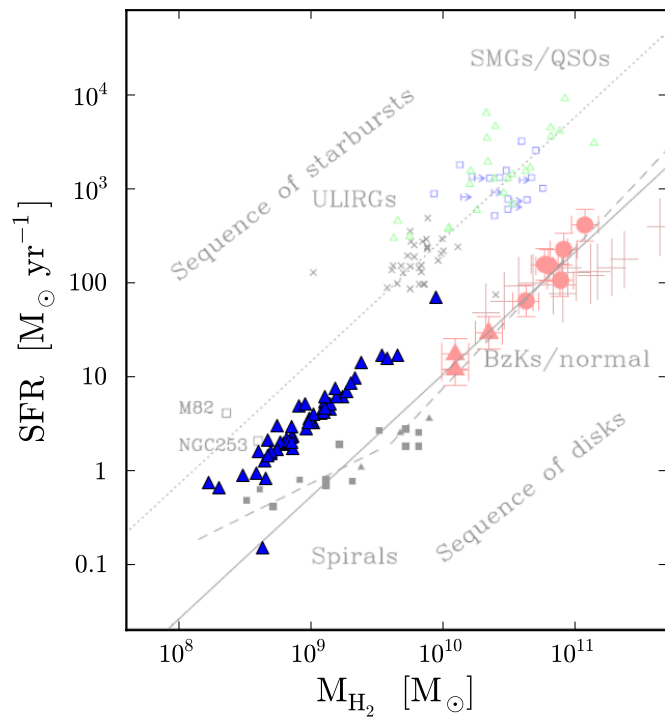
Figure 4. Comparison of the relation between total SFR and total H$_2$ mass for galaxies in the KMT09 simulation at $z = 4$ (blue triangles) with the observational results from Daddi et al. (2010, their Figure 1) for lower redshift galaxies. The simulation and observations have relations with similar slopes, and the simulated galaxies lie in between the "sequence of starbursts" and "sequence of disks." Higher SFR for a given H$_2$ mass may be expected for lower metallicity systems, which require higher densities to allow the transition to H$_2$ to occur.

(A color version of this figure is available in the online journal.)

Figure 5. Simulated mean Kennicutt–Schmidt relations for standard SF with three different density thresholds, $n_{thresh} = 5,\ 50,\ 500$ cm^{-3}, and the H$_2$-regulated SF. The KT07 and KMT09 lines are from the $z = 4$ output, the KT07_low and KT07_high ones from $z = 6$.

(A color version of this figure is available in the online journal.)

in the ∼10 Myr over which they produce significant ionizing luminosities that may be detected in Hα or other nebular emission lines. Typical velocity dispersions, however, may well be larger at higher redshift (see Cresci et al. 2009 for some empirical evidence for this), as expected if they are set by cosmological accretion (Krumholz & Burkert 2010) instead of

cold disk dynamics. In fact, we find that averaged on 1 kpc scales our galaxies have a mean 1D stellar velocity dispersion[7] of 44 km s^{-1} at $z = 4$. In 5% of all cells (19 in total) the 1D stellar velocity dispersion exceeds 100 km s^{-1}. At these velocities wandering becomes more important, and as a result an increased scatter in the KS relation should be expected at high redshift. We have verified that the amount of scatter at low Σ_{gas} increases when we reduce the spatial averaging scale of the

---

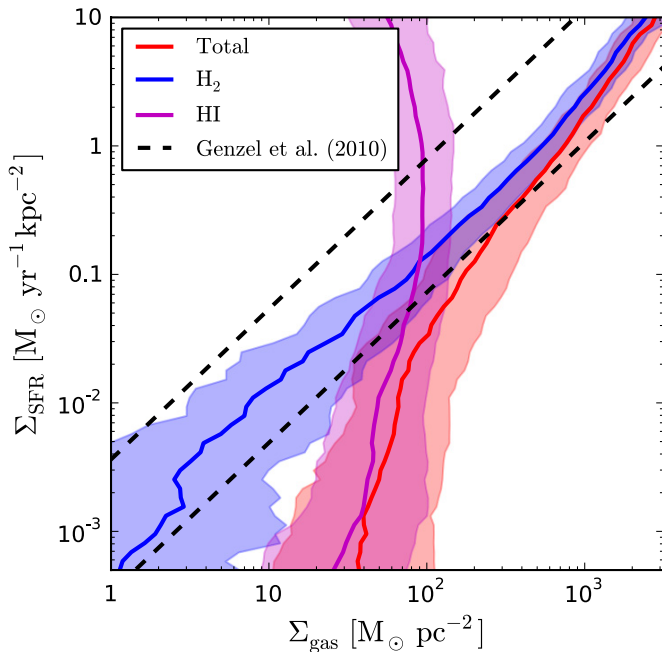[7] We only include cells containing more than 10 star particles in the average.

Figure 6. Kennicutt–Schmidt relation for total (red), H_2 (blue), and H I (magenta) surface density from the KMT09 simulation at $z = 4$. The solid lines indicate the mean relations from the simulations, the shaded regions cover the central 68% scatter (16th–84th percentile), and the two dashed lines are the best-fit Σ_{H_2}–Σ_{SFR} relations reported by Genzel et al. (2010) for their $z = 0$–3.5 samples of "normal" SF galaxies (lower line) and luminous mergers (LIRGs/ULIRGs and SMGs, upper line).

(A color version of this figure is available in the online journal.)

Figure 7. Total gas KS relation for simulated galaxy subsamples split by their mean gas-phase metallicity, from the KMT09 simulation at $z = 4$. Solid lines indicate the mean relations from the simulations, and the shaded regions cover the central 68% scatter (16th–84th percentile). The lower the metallicity, the higher the Σ_{gas} that is needed for the transition to fully molecular gas, which corresponds to the turnover in the KS relation.

(A color version of this figure is available in the online journal.)

surface density maps (see Figure 9) or increase the temporal SF timescale $t_\star$ (see also Feldmann & Gnedin 2011).

In Figure 6 we compare the KS relations for the total, atomic, and molecular gas in the KMT09 simulation. The H_2 relation does not exhibit a cutoff at low column densities, since we have not imposed any explicit density threshold in the H_2-regulated SF prescription. The H_2 relation is shallower than the total gas one, and its slope is in excellent agreement with the observational determination of the slope of the molecular gas KS relation by Genzel et al. (2010). These authors studied a population of "normal" star-forming galaxies at $z = 0$–3.5 and a population of luminous $z \sim 0$ and $z \sim 1$–3.5 mergers (LIRGs/ULIRGs and SMGs) and found that both had equal H_2 KS slopes of 1.17 with about a 1 dex higher normalization for the luminous merger sample. The two best-fit relations from their work are shown as dashed lines in Figure 6, and our H_2 KS relation lies right in between the two. The H I relation instead is much steeper and does not extend much beyond 70 $M_\odot$ pc^{-2}. The near constant offset at low Σ_{gas} between the total gas and H I KS relations is due to the presence of a significant amount of ionized gas on ∼kpc scales. The overall picture matches the results reported by GK10 and is in qualitative agreement with the empirical findings reported by Bigiel et al. (2008), confirming that the origin of the turnover in the total gas KS relation is indeed the transition from predominantly atomic to fully molecular gas.

3.2. Metallicity Dependence

The KS cutoff occurs at somewhat higher Σ_{gas} in both KT07 and KMT than in the observational data from Bigiel et al. (2008). This can be understood as a result of the lower metallicities in our simulated galaxies. We split our 35
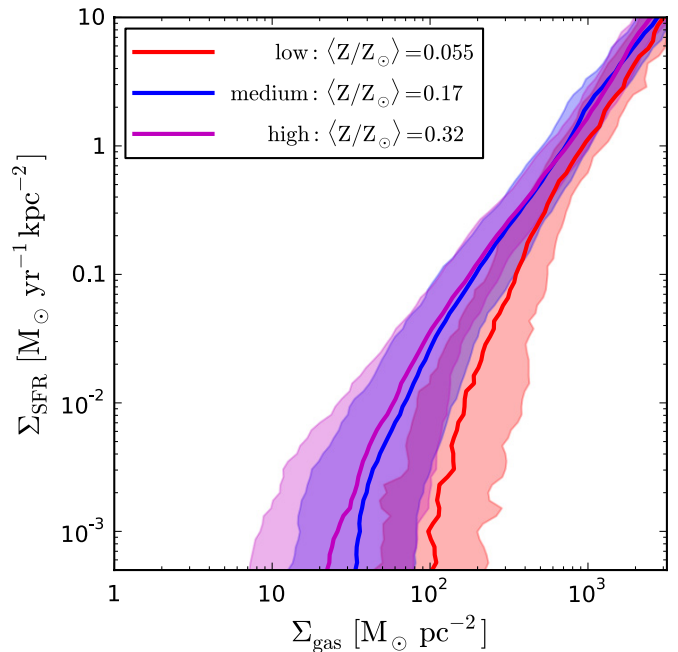
galaxy sample into three subsamples of different mean gas-phase metallicities, $\langle Z/Z_\odot \rangle = 0.055$, 0.17, and 0.32. Each subsample contains at least 10 galaxies. The highest metallicity galaxy has $Z = 0.56\,Z_\odot$, considerably below the closer-to-solar metallicity sample of $z = 0$ field galaxies analyzed by Bigiel et al. (2008). The lower the metallicity of the gas, the higher the total gas surface density that is required in order to provide enough LW shielding to allow the transition to fully molecular gas. The Σ_{gas} scale at which the KS cutoff occurs is thus expected to scale inversely with metallicity, and this is exactly what Figure 7 shows. The cutoff in the KS relation shifts to progressively higher Σ_{gas} for decreasing mean metallicity, occurring at $\gtrsim 100\,M_\odot$ pc^{-2} for the lowest metallicity case. A similar trend was previously reported by GK10. Recent observations of SF in the Small Magellanic Cloud (SMC) show that the break in the total gas SF law is indeed shifted to higher surface density by a factor of $Z_\odot/Z_{SMC} \sim 5$, in precisely the manner that our models predict (Bolatto et al. 2011). The higher Σ_{gas} cutoff in the KS relation for low-metallicity systems may also be responsible for the observational results that Σ_{SFR} in damped Lyα (DLA) systems (Wolfe & Chen 2006) and Lyman break galaxies (Rafelski et al. 2009, 2011) at $z \approx 3$ appears to lie well below the $z = 0$ KS relation (see GK10 for a more in-depth exploration of this possibility).

The success of our model at capturing the physics governing the gas-phase structure in dwarf galaxies is further demonstrated by Figure 8. There we compare the H_2 fraction ($\Sigma_{H_2}/\Sigma_{H I}$) as a function of total neutral hydrogen gas column ($\Sigma_{H I} + \Sigma_{H_2}$) for the low-metallicity galaxy sample ($\langle Z \rangle = 0.055\,Z_\odot$) with observational data for the SMC that has recently become available. Bolatto et al. (2011) have determined an H_2 column density map of the SMC at ∼12 pc resolution by combining *Spitzer* IR measurements and radio (ATCA and Parkers) H I data.
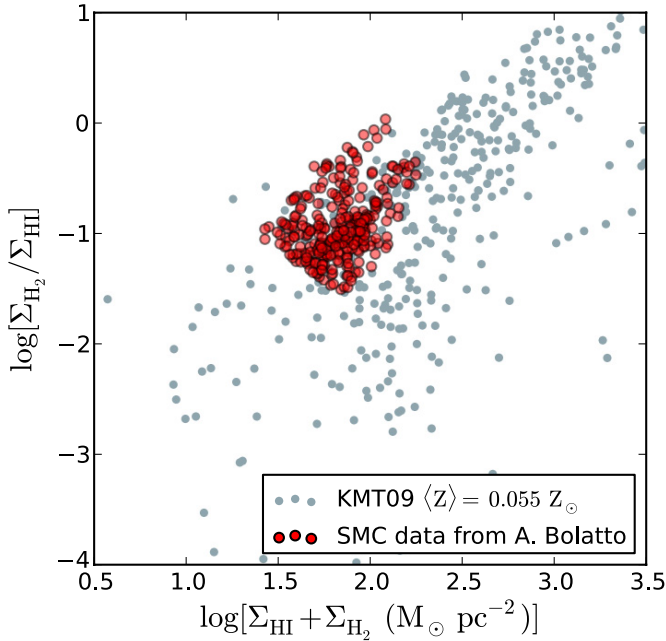
Figure 8. Comparison of the H_2-to-H I ratio vs. total neutral hydrogen column density ($\Sigma_{H I} + \Sigma_{H_2}$) between SMC data smoothed at 200 pc (from Bolatto et al. 2011) and low-metallicity gas in the KMT09 simulation at $z = 4$ also smoothed at 200 pc. The overlap between simulated and observational data indicates that our model does an adequate job of capturing the atomic-to-molecular transition in real dwarf galaxies.

(A color version of this figure is available in the online journal.)

In Figure 8 we compared their data smoothed on ~200 pc scale (kindly provided by A. Bolatto) to our $z = 4$ KMT09 simulation data smoothed at the same scale. There is good overlap between simulation and observational data, but in our simulations the distribution of points extends both to higher total gas columns and to lower H_2 fractions than probed by Bolatto et al. (2011).

3.3. Smoothing Scale Dependence

In Figure 9 we show the dependence of the total gas and H_2 KS relations on the spatial scale over which the data is smoothed. In addition to our fiducial scale of 200 pc, we present the relations for up to twenty times finer and five times coarser smoothing. This smoothing scale range roughly mimics the variations in the angular resolution (i.e., beam size) of the radio observations used to establish the observational KS relation, ranging from spatially resolved measurements of nearby spiral galaxies with sub-kpc resolution (Kennicutt et al. 2007; Bigiel et al. 2008) to high-redshift observations in which a large fraction of the galaxy is contained in a single beam (Kennicutt 1998). We do not see much evidence for a smooth scale dependence, in either total gas or H_2 KS relations. The scatter in the relations, however, increases for smaller smoothing scales, in agreement with observations (Schruba et al. 2010; Liu et al. 2011).

3.4. Resolution Dependence

With only seven levels of AMR, our simulations are unable to resolve the true Jeans length of the cold, molecular gas in star-forming galaxies. As discussed in Section 2, we resort to an artificial minimum pressure support in order to stabilize gas cells at the highest refinement level against artificial fragmentation. This has the undesirable consequence of making the results of our simulations somewhat dependent on resolution, since additional levels of refinement will allow gas to collapse further and reach higher densities, until the resolution becomes adequate to resolve the true Jeans length. Unfortunately, additional refinement levels come at a computational cost. To run the KMT09_L8 simulation, a clone of KMT09 with one additional refinement level ($l_{max} = 8$), down to $z = 6$ took about three times as long as the KMT09 run. Note that virtually every $l = 7$ KMT09 grid was at least partially further refined in KMT09_L8.

In the left panel of Figure 10 we show a comparison of the distribution functions of number density in the maximally
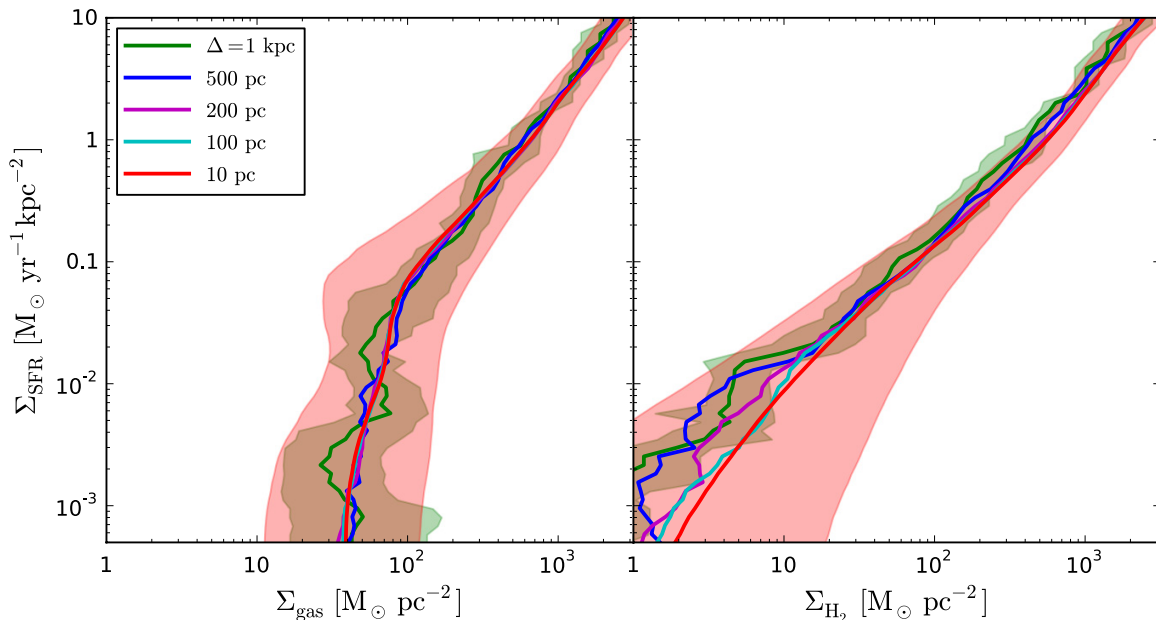

Figure 9. Dependence of the total gas (left) and H_2 (right) KS relation on the smoothing scale Δ in the KMT09 simulation at $z = 4$. The solid lines show the mean relations, and the shaded regions cover the central 68% scatter (for clarity we only show the scatter for $\Delta = 10$ and 1000 pc). The mean relation does not show much dependence on averaging scale, but the scatter increases toward smaller Δ, in agreement with observations (Schruba et al. 2010; Liu et al. 2011).

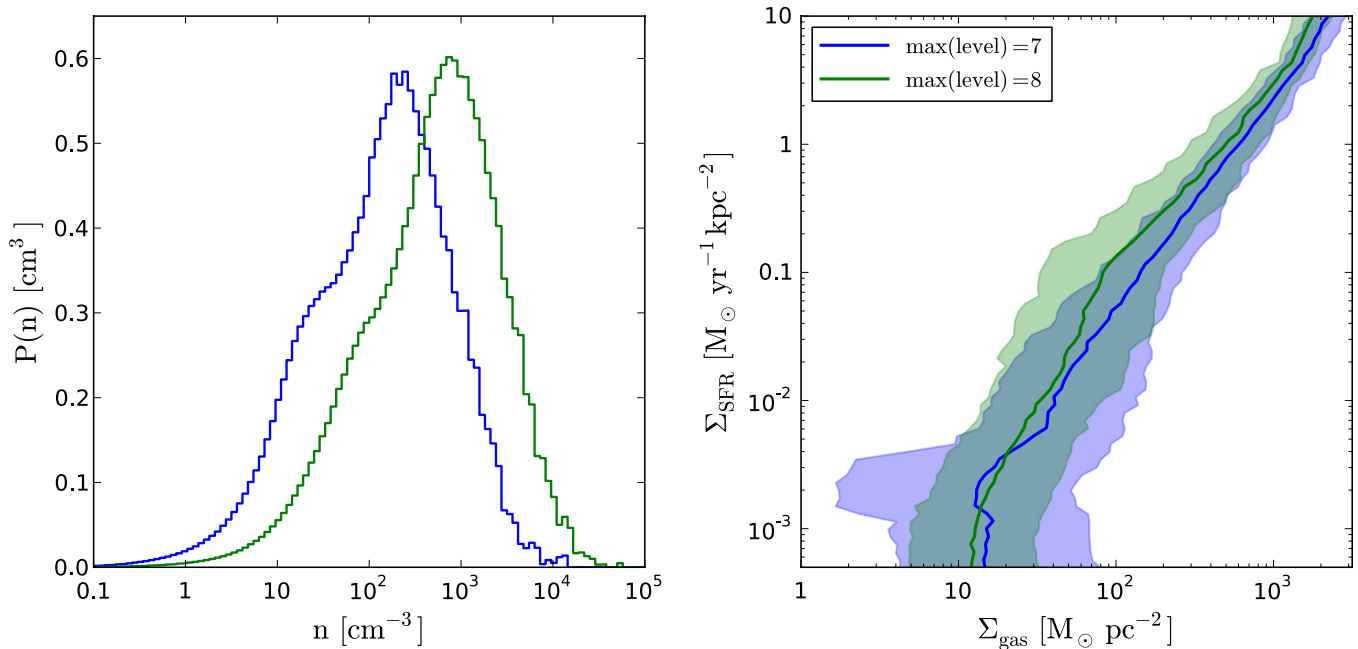(A color version of this figure is available in the online journal.)

Figure 10. Left: probability distribution functions of the proper gas number density in the KMT09 and KMT09_L8 simulations at $z = 6$ for cells at the maximum refinement level ($l_{max} = 7$ and 8, respectively). Right: the corresponding total gas KS relation. The additional refinement level allows gas in KMT09_L8 to reach higher densities, which in turn results in greater SFR densities and an increase in the normalization of the KS relation.

(A color version of this figure is available in the online journal.)

refined grid cells in the KMT09 and KMT09_L8 simulations at $z = 6$. The additional refinement level has allowed gas to collapse to higher densities. The mean density at $l = 7$ is 427 cm^{-3} in the KMT09 simulation, but 1420 cm^{-3} at $l = 8$ in KMT09_L8. Higher densities will lead to larger SFR and an increase in Σ_{SFR}. Σ_{gas} smoothed on ~kpc scales, however, will be unaffected, since it depends only on the *total mass* enclosed in a given l_{avg} cell, not the local density. It is not surprising, then, that the simulated KS relation (right panel of Figure 10) shows that the KMT09_L8 KS relation has somewhat higher amplitude than in KMT09.

It is important to note that, despite its higher resolution, model KMT09_L8 is not necessarily more realistic than KMT09, because it lacks the physics needed to properly model molecular clouds at the increased resolution. In the absence of feedback mechanisms other than supernovae, increasing resolution allows the gas to collapse to ever-higher density, so that the bulk of the molecular gas will always reside near the resolution limit. However, this behavior is not realistic. In observed nearby galaxies, the bulk of the molecular clouds exist at densities of a few hundred cm^{-3} rather than a few thousand cm^{-3} (i.e., closer to the mean in KMT09 than KMT09_L8; Blitz 1993), and molecular cloud properties are independent of galactic environment, strongly suggesting internal regulation (Bolatto et al. 2008). Possible mechanisms to provide this regulation include ionized gas pressure (Matzner 2002; Krumholz et al. 2006; Goldbaum et al. 2011), protostellar winds (Nakamura & Li 2007; Wang et al. 2010), and radiation pressure (Krumholz & Matzner 2009; Murray et al. 2010; Fall et al. 2010; Hopkins et al. 2011), none of which are included in our simulations. Thus, we regard the KS law we obtain from KMT09 as at least as reliable as the one we obtain from KMT09_L8. Moreover, this comparison yields an important caution: increasing resolution without a corresponding increase in physics does not necessarily yield a better result.

4. STELLAR MASS FRACTION

We now turn to the effects of an H$_2$-regulated SF prescription on the stellar content of the dark matter halos in our simulations. In Figure 11 we show plots of the stellar mass fraction $f_\star = M_\star/M_h$ against the total halo mass $M_h = M_{DM} + M_{gas} + M_\star$ for simulations with a standard (KT07) and H$_2$-regulated (KMT09_ZFz10[8]) SF prescription. In the normal SF case (left panel), halos with total masses as low as $10^9 M_\odot$ have been able to form a substantial stellar content, with values of $f_\star$ not dropping much below 1%. This is problematic in view of the observational dearth of such dwarf galaxies in the local universe. Given the high volume density of $M > 10^9 M_\odot$ dark matter halos predicted by ΛCDM structure formation, such a high SF efficiency would vastly overproduce the faint end of the field dwarf galaxy LF and the abundance of faint Local Group dwarf galaxies.

In Via Lactea II, a collisionless simulation of the formation of a Milky Way's dark matter halo (Diemand et al. 2008), for example, there are ~100 halos with an identifiable $z = 0$ remnant within the host halo's virial volume that had a mass exceeding $10^9 M_\odot$ at some point in their evolution. Yet of the Milky Way dwarf satellite galaxies, probably only the two Magellanic Clouds, Fornax and Leo I (and possibly the progenitor of the Sagittarius dwarf), have a stellar mass greater than $10^7 M_\odot$. The vast majority of such dark matter halos must thus have SF efficiencies well below 1% (Rashkov et al. 2012). The same is true of faint field galaxies, not just satellites. Comparisons of the local universe galaxy LF from Sloan Digital Sky Survey with the predicted dark matter field halo mass function show that at $z < 1$ the stellar mass fraction must have a maximum of ~0.01–0.03 around $10^{12} M_\odot$, decreasing sharply

---

[8] We now focus on KMT09_ZFz10, because the slightly earlier metallicity floor ($z = 10$, instead of $z = 9$ in KMT09) results in a more gradual suppression of $\langle f_\star \rangle$; see Section 4.3.
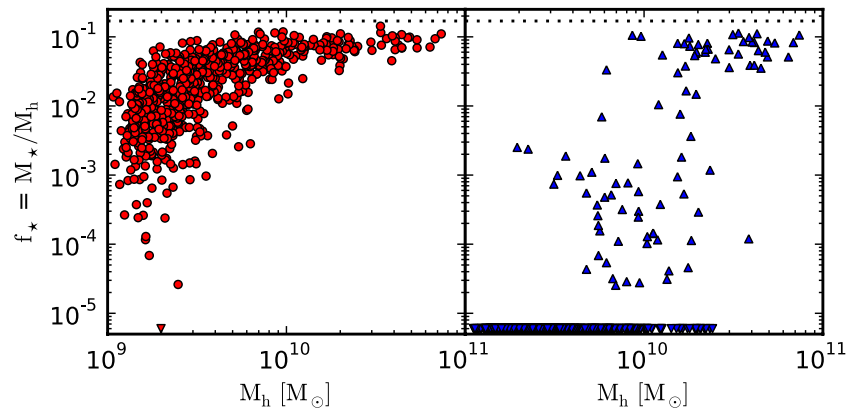
Figure 11. Stellar mass fraction $f_\star$ vs. total halo mass in a simulation with standard SF (KT07, left) and with H_2-regulated SF (KMT09_ZFz10, right) at $z = 4$. The dotted horizontal line indicates an $f_\star$ equal to the cosmic baryon fraction Ω_b/Ω_M, i.e., a 100% gas-to-star conversion efficiency.

(A color version of this figure is available in the online journal.)

toward lower masses (Zheng et al. 2007; Conroy & Wechsler 2009; Guo et al. 2010; Moster et al. 2010; Behroozi et al. 2010).

The most commonly invoked mechanisms to lower the stellar mass fraction in these low-mass galaxies are (1) the prevention of gas cooling due to the meta-galactic UV background (Efstathiou 1992; Kauffmann et al. 1993; Bullock et al. 2000) and (2) stellar feedback from massive winds and supernovae (Larson 1974; Kauffmann et al. 1993; Benson et al. 2002). Our simulations include a model for the UV background, via a spatially uniform, optically thin radiation field that accounts for the UV emissivity from both quasars and galaxies[9] (Haardt & Madau 2001). By itself this feedback does not appear to be able to suppress SF in 10^9–10^{10} $M_\odot$ halos at $z > 4$ in our simulations. As discussed in Section 2.3, we do include a supernova feedback prescription in our simulation, but in a form known to be insufficiently strong to effect the necessary reduction in SF efficiency or to reproduce observed galactic outflows. This is exemplified by the high stellar mass fractions ($f_\star \approx 0.06$, a factor 5–10 higher than what is allowed by observational constraints at much lower redshift, $z \lesssim 1$) even in our most massive halos (10^{10}–10^{11} $M_\odot$) (see also Avila-Reese et al. 2011).

It is reasonable to expect a similar, or even greater, suppression of $f_\star$ for lower mass halos, whose shallower potential wells should make it easier for winds and supernovae to expel their gas. However, Font et al. (2011) find that in order to simultaneously match the LF of Local Group dwarf galaxies and their observed mass–metallicity relation, the strength of stellar feedback must saturate in halos with $V_{\max} \lesssim 65$ km s^{-1} ($\approx 5 \times 10^{10}$ $M_\odot$). Furthermore, a physically realistic modeling of stellar feedback processes in cosmological numerical simulations is beyond current computational capabilities, and it remains unclear how well the various sub-grid physics implementations discussed in the literature actually capture the true nature of this feedback. Although we do not doubt that stellar feedback processes play an important role in regulating SF in low-mass halos, we now show that regulating SF by the H_2 abundance may play an equally important role in lowering stellar mass fractions in low-mass ($<10^{10}$ $M_\odot$) halos, as previously suggested by G09 and GK10.

The right panel of Figure 11 shows that our H_2-regulated SF prescription introduces a threshold below which the stellar mass content of halos is strongly suppressed. At halo masses greater than 10^{10} $M_\odot$, the SF efficiency is only mildly reduced, dropping

from $\langle f_\star \rangle = 0.062$ to 0.035. Between 5×10^9 $M_\odot$ and 10^{10} $M_\odot$, only a small fraction of halos (about 10%) has been able to form stars and only with reduced SF efficiency, and at even lower halo masses SF has been almost completely suppressed. We visually demonstrate this suppression in Figure 12, where we show direct comparisons of the baryonic structure ($\Sigma_\star$, Σ_{gas}, Σ_{H_2}, and density-weighted metallicity) between the KT07 and KMT09_ZFz10 simulations for two representative halos: one high-mass halo ($M_h = 2.0 \times 10^{11}$ $M_\odot$), in which H_2-regulation has not had a big effect, and one low-mass halo ($M_h = 5.8 \times 10^9$ $M_\odot$), in which the stellar mass fraction has been suppressed by nearly one order of magnitude from $f_\star = 0.057$ to 0.0069. Many more halos like these exist in our simulations.

Figure 13 shows the baryonic content of halos in KT07 and KMT09 as a function of their mass. We plot mean mass fractions in M_h-bins of width 0.25 dex of the total baryonic content, stars, neutral gas (H I + He I + H_2), ionized gas (H II + He II + He III), H_2, and metals. The total baryonic mass fraction remains equal to the cosmic mean down to $\sim 2 \times 10^9$ $M_\odot$. The slight drop in the total baryonic and neutral gas fractions at lower halo masses can be attributed to the meta-galactic UV background, which is able to ionize and heat most of the gas, preventing it from falling into the halo. The mass fractions of H_2, metals, and stars roughly trace each other. In KT07, the stellar mass fraction decreases gradually from ~ 0.4 of the cosmic baryon fraction at $M_h = 10^{11}$ $M_\odot$ to 0.25 at 10^{10} $M_\odot$, before the combined actions of UV background and (weak) supernova feedback further reduce it to ~ 0.01 at 10^9 $M_\odot$. In KMT09, on the other hand, the stellar mass fraction is suppressed already at much higher halo masses, dropping below 0.1 of the cosmic mean at 10^{10} $M_\odot$ and cutting off completely at 4×10^9 $M_\odot$. Note that because we have included halos with $M_\star = 0$ in the calculation of the mean $f_\star$, it should not be viewed as a typical value for any individual halo, but as a population average. With H_2 regulation the SF is quenched in low-mass halos without heating and removing much of the gas, contrary to the effects of efficient supernova feedback.

Why should a locally H_2-regulated SF prescription be sensitive to the total halo mass? Recall that with the two-phase equilibrium assumption (KMT09 model), the local H_2 abundance is completely determined by the H I column density and the metallicity of the gas. A reduced SF efficiency in low-mass halos could thus be due to either lower column densities or lower metallicities than in more massive halos, or a combination of the two.

---

[9] The galactic contribution dominates the UV background at this early epoch.
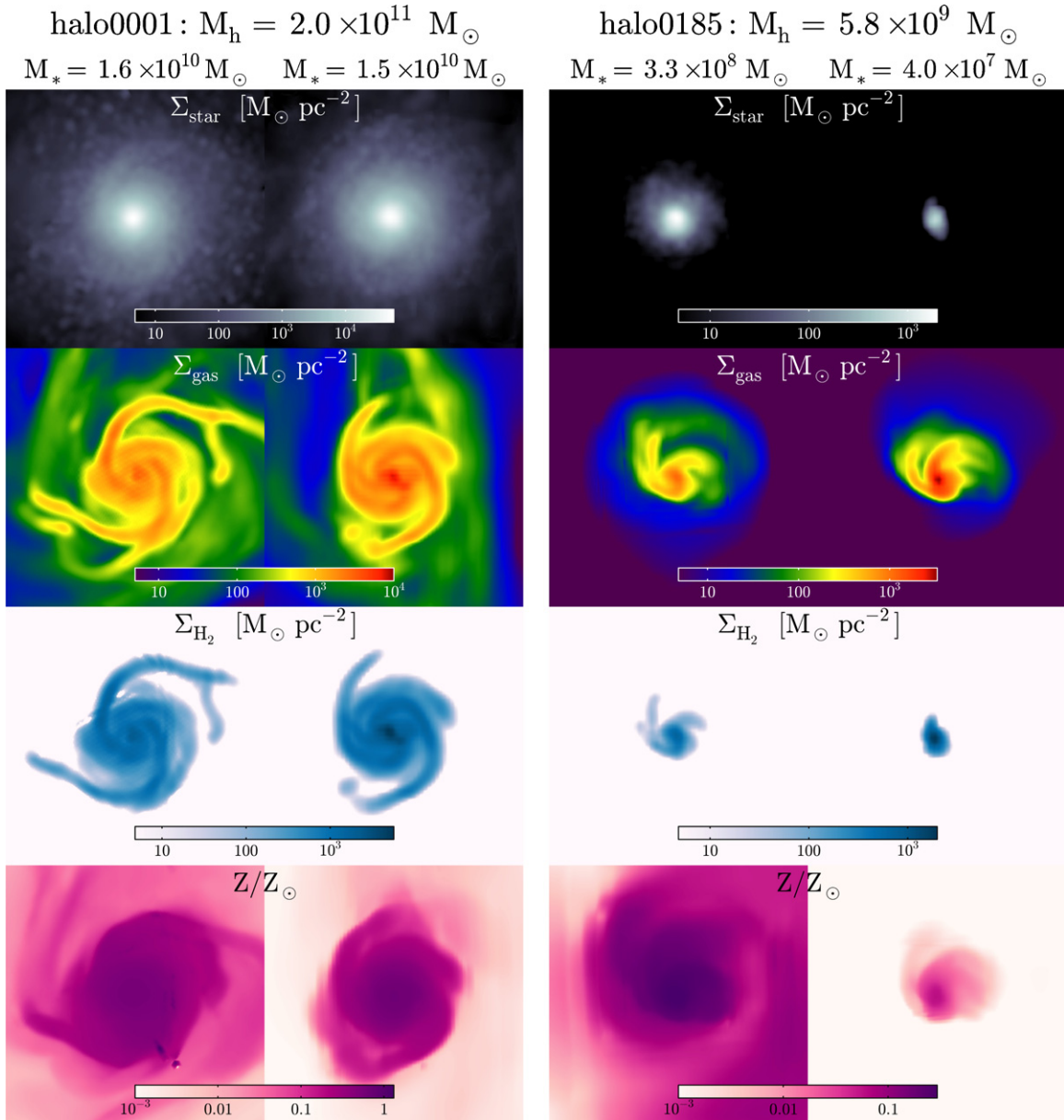
Figure 12. Comparison of the baryonic structure of two identical halos, one with high total mass (halo0001, left panel) and one with low total mass (halo0185, right panel), between the KT07 (left columns) and KMT09_ZFz10 (right columns) simulations at $z = 4$. From top to bottom, we show surface densities of stellar mass, total gas, and H_2, and a density-weighted projection of metallicity, in a 5×5 kpc region centered on the galaxies. These are merely two representative halos, and many more like them exist in our simulations. The stellar content is greatly suppressed in the KMT09 low-mass halo.

(A color version of this figure is available in the online journal.)

Figure 14 reveals that lower metallicities are primarily responsible. The figure shows two-dimensional (2D) volumetric probability density functions (phase diagrams) of total gas column density Σ_{gas} and metallicity Z, for $l = 7$ grid cells in $M < 10^{10} M_\odot$ (left panel) halos and $M > 10^{10} M_\odot$ (right panel) halos. The color scale indicates the volume fraction at a given (Σ_{gas}, Z), and the diagonal lines represent contours of constant f_{H_2}, according to the KMT09 prescription. The 1D distributions at the top and sides of the figure show that while both low- and high-mass halos have comparable column density distributions, the metallicity distribution peaks at $Z/Z_\odot \approx 0.25$ for the high-mass halos, but at $Z/Z_\odot = 10^{-3}$ for the low-mass halos. Recall that we imposed a $Z/Z_\odot = 10^{-3}$ metallicity floor at $z = 9$, so this indicates that low-mass halos typically remain unenriched. This lack of metals in low-mass halos is responsible

for a reduced H_2 abundance and hence a suppressed stellar mass fraction.

As we discuss in the remainder of this section, a number of factors, both of physical nature and pertaining to the limitations of our simulations, affect the mass scale and the degree of the $f_\star$ suppression due to H_2-regulated SF. A complete suppression of SF in halos with masses below $5 \times 10^9 M_\odot$ is too strong of an effect to reproduce the LF of Local Group satellites, many of which are consistent with having formed in $\lesssim 10^9 M_\odot$ halos (Madau et al. 2008). In this work, we demonstrate that H_2-regulated SF can have important consequences for the SF efficiency in low-mass halos, but we openly acknowledge that the true nature of this suppression will depend on details of the SF processes, stellar feedback, and metal enrichment that are not captured with sufficient fidelity in our simulations.
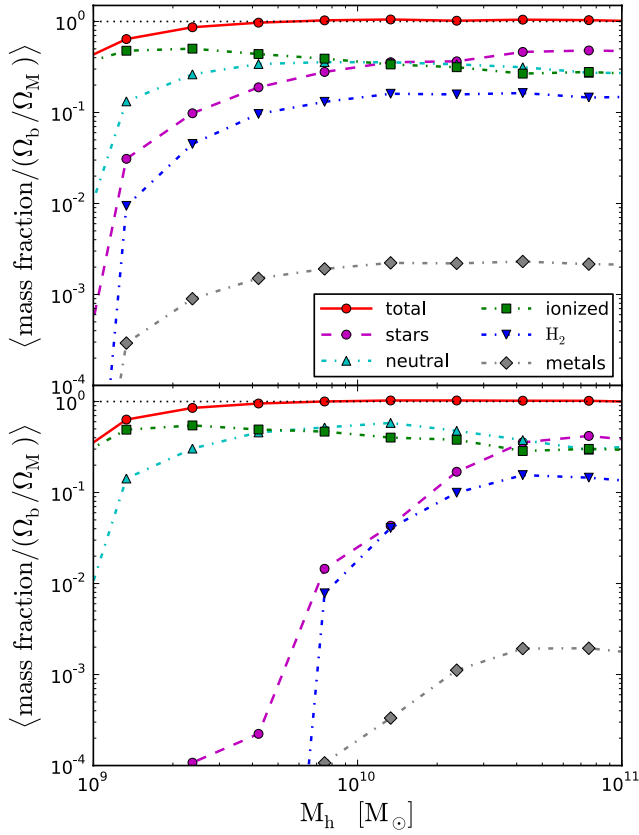
Figure 13. Baryonic content of halos vs. their total mass, for the KT07 (top panel) and KMT09_ZFz10 (bottom panel) simulations at $z = 4$. We show mean mass fractions normalized to the cosmic baryon fraction (Ω_b/Ω_M) in M_h-bins of width 0.25 dex for the total baryonic content (stars + all gas + metals; solid lines with circles), stars (dashed with circles), neutral gas (H I + He I + H_2; dot-dashed with upward triangles), ionized gas (H II + He II + He III; dot-dashed with squares), H_2 (dot-dashed with downward triangles), and metals (dot-dashed with diamonds). Note that although an H_2 curve is plotted in the KT07 panel, H_2 has no effect in that simulation.

(A color version of this figure is available in the online journal.)

4.1. Dependence on Two-phase Equilibrium

The assumption of two-phase equilibrium between a CNM, hosting molecular clouds and SF, and the surrounding WNM is not uncontroversial. As discussed in Krumholz et al. (2009), shocks from supernova explosions or supersonic ISM turbulence, for example, likely temporarily drive the surrounding gas out of pressure balance, in which case the typical gas density could differ significantly from the value estimated from two-phase equilibrium. The time to re-establish equilibrium between a CNM and WNM can be comparable (few Myr; Wolfire et al. 2003) to the shock recurrence timescale, and hence it is prudent to consider the effects of the KMT09 model without the two-phase equilibrium assumption.

In this case the molecular hydrogen fraction is no longer independent of the H_2-dissociating LW background, and absent a full radiation transfer treatment (G09) we need to externally specify its intensity. For computational ease we have considered here only the case of a constant, spatially uniform LW intensity. Of course, it would be preferable to tie the LW intensity to the local SFR, averaged over ∼kpc scales and tens of Myr, but we defer the investigation of this more realistic treatment to future work.

In Figure 15 we show $\langle f_\star \rangle$ versus M_h at $z = 5$ for simulations KMT09_FLW{1, 10, 100, 1000}, with values of the LW intensity ranging from 1 to 1000 times the $z = 0$ Milky Way value of 7.5×10^{-4} LW photons cm^{-3} (Draine 1978). For clarity we have plotted the mean values of $f_\star$ in bins of M_h of width 0.25 dex. The means include halos with $f_\star = 0$, which implies that these values of $\langle f_\star \rangle$ should thus be viewed as population averages, rather than representative values for any individual halo. The results from the standard SF (KT07) and the two-phase equilibrium (KMT09) simulations are included for comparison. The lowest LW intensity case (KMT09_FLW1) is almost indistinguishable from the standard SF model. In this case the dissociating flux is not strong enough to affect the H_2 abundance even in the lowest mass halos. As the intensity
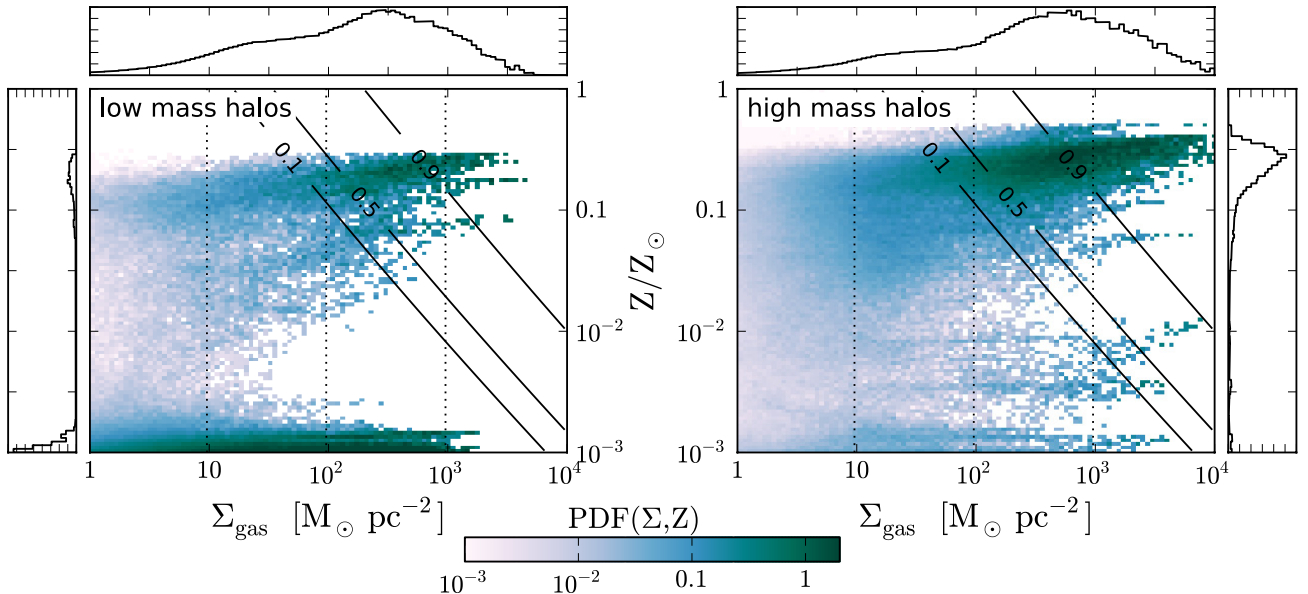

Figure 14. 2D phase diagrams of Σ_{gas} vs. Z determined at $l_{max} = 7$ in the KMT09 simulation at $z = 5$, for low-mass ($M < 10^{10} M_\odot$, left panel) and high-mass ($M > 10^{10} M_\odot$, right panel) halos. Contours of constant f_{H_2} (at 0.1, 0.5, and 0.9) are plotted with solid lines. For reference we show with dotted lines the column densities corresponding to the 3D density thresholds employed in the KT07 ($50\ cm^{-3}$), KT07_low ($5\ cm^{-3}$), and KT07_high ($500\ cm^{-3}$) simulations. The majority of gas in low-mass halos has very little or no H_2, and this appears to be primarily due to lower metallicities, not lower column densities.

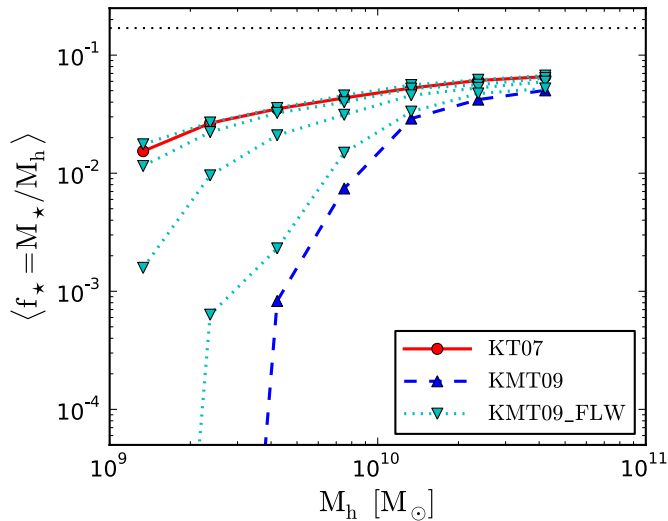(A color version of this figure is available in the online journal.)

Figure 15. $\langle f_\star \rangle$ vs. M_h at $z = 5$ for the four KMT09 simulations without the two-phase equilibrium assumption and a spatially uniform Lyman–Werner radiation field with intensity equal to 1, 10, 100, 1000 times the mean Milky Way value (dotted lines with downward triangles; increasing LW intensity from top to bottom). We plot the mean of $f_\star$ in M_h-bins of width 0.25 dex. The means include halos with $f_\star = 0$. For comparison we also show the original KT07 (solid line with red circles) and two-phase equilibrium KMT09 results (dashed line with upward triangles). Note that for the KMT09_FLW simulations (but not for KMT09) we apply a "clumping factor" of 30 to the H_2 formation rate (see the text for details).

(A color version of this figure is available in the online journal.)

of the LW background is increased, the halo mass at which H_2 formation begins to be suppressed increases in proportion. At 1000 times the Milky Way's LW intensity (lowest dotted line), the suppression mass almost reaches the value in the two-phase equilibrium model. Recall that the KMT09_FLW simulations were run with an effective sub-grid clumping factor of 30 $((\sigma_{d,-21}/\mathcal{R}_{-16.5}) = 1/30)$, and the resulting enhanced H_2 recombination rate is partially responsible for the reduced SF suppression compared to the two-phase equilibrium simulation. However, while the absolute strength of the SF suppression in the simulations without two-phase equilibrium is sensitive to the value of the clumping factor, the trend with the intensity of the LW background is not.

4.2. Resolution Dependence

In Figure 16 we compare $f_\star$ versus halo mass for the KMT09_L8 simulation to the results from KT07 and KMT09. While there still is a suppression of SF in low-mass halos compared to KT07, the scale at which this suppression occurs has shifted to lower masses, around $3 \times 10^9\, M_\odot$. Considering our earlier finding (Section 3.4) that the additional resolution increases the SF rates in KMT09_L8, it is perhaps not surprising that the $f_\star$ suppression mass scale also exhibits some resolution dependence. In this case the sensitivity to the maximum resolution arises because the increase in density afforded by the additional refinement level exceeds the factor of two reduction in grid cell width, thus leading to a net increase in column densities on the finest grid cells. The enhanced LW shielding eases the transition to the molecular phase and allows SF to occur in lower mass halos.

The exact value of this transition will depend on the details of the SF and stellar feedback processes on scales below our current resolution limit, as we discussed in Section 3.4. However, our fiducial $l_{\max} = 7$ grid resolution of $76.3 \times 5/(1+z)$ proper parsec
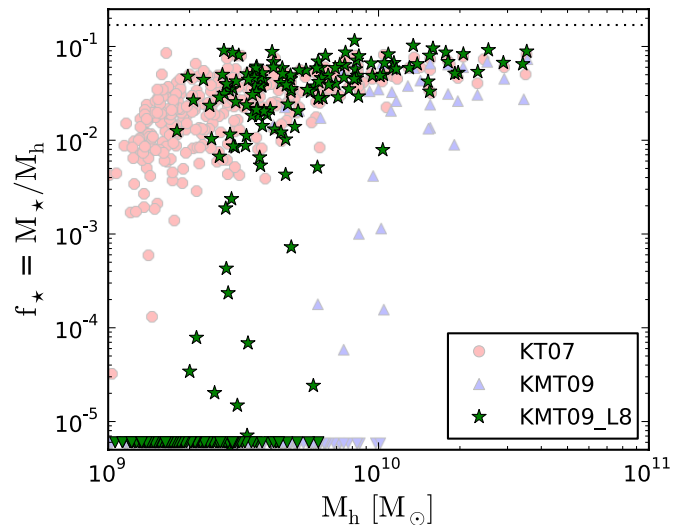

Figure 16. $f_\star$ vs. halo mass (at $z = 6$) for the KMT09_L8 simulation, which has one additional refinement level compared to KMT09 and KT07. The halo mass scale at which star formation is suppressed due to the inability of gas to become molecular is lower than in the KMT09 simulation. The true value of this suppression mass scale in nature will depend on the strength of stellar feedback, metal mixing, and other processes not resolved in our simulations.

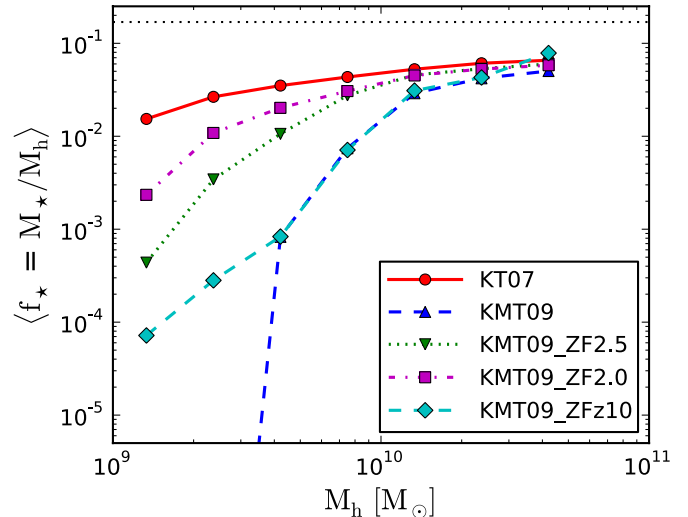(A color version of this figure is available in the online journal.)

Figure 17. Dependence of $\langle f_\star(M_h) \rangle$ at $z = 6$ on the metallicity floor. We plot the mean of $f_\star$ in M_h-bins of width 0.25 dex at $z = 6$ for KT07 (solid lines with circles) and three versions of KMT09 with increasing values of the $z = 9$ metallicity floor, $[Z_{\mathrm{floor}}] = -3.0$ (dashed line with upward triangles), -2.5 (dotted with downward triangles), and -2.0 (dot-dashed with squares), and one case with $[Z_{\mathrm{floor}}] = -3.0$ applied at $z = 10$ (dashed with diamonds). The means include halos with $f_\star = 0$. Note that a simulation with $\log_{10}(Z_{\mathrm{floor}}/Z_\odot) = -4.0$ at $z = 9$ produced no stars at all.

(A color version of this figure is available in the online journal.)

is comparable to the observed size of giant atomic–molecular cloud complexes, and our $l = 7$ grid-cell-averaged densities (Figure 10, left panel) are in good agreement with observational estimates of their average densities (Blitz 1993). We thus believe that the resolution of our fiducial simulations ($l_{\max} = 7$) is well matched to the problem we are studying.

4.3. Metallicity Floor Dependence

In Figure 17 we show how the $f_\star$ suppression depends on the amplitude and time of the metallicity floor that we impose early

in the simulations to mimic the enrichment from Population III supernovae. Higher values of $[Z_{\rm floor}]$ and an earlier time allow SF to occur in lower mass halos. Note that the KMT09_ZF4.0 simulation ($[Z_{\rm floor}] = -4.0$) produced no stars at all. Imposing the metallicity floor at $z = 10$ instead of $z = 9$ has the particularly interesting result of allowing a small amount of SF in very low mass halos ($M_h < 5 \times 10^9 \, M_\odot$), which may help to alleviate the tension with the faint end of the Local Group satellite galaxy LF.

For a given $Z_{\rm floor}$, a halo's ability to form stars is determined by the highest column densities that its gas can condense to prior to the enrichment from the first star particles in our simulation. Gas in more massive halos is able to reach higher column densities, owing to their earlier collapse times and deeper potentials. Below some halo mass scale, gas will not be able to reach sufficiently high column densities to turn molecular and allow SF to occur. The necessary column densities depend on metallicity: at $[Z] \equiv \log_{10}(Z/Z_\odot) = -3.0$, gas must reach a column density of 6.7×10^3 (1.4×10^4, 8.0×10^4) $M_\odot$ pc^{-2} in order to be 10% (50%, 90%) molecular. At $[Z] = -2.5$ the required column is reduced to 2.3×10^3 (4.9×10^3, 3.0×10^4) $M_\odot$ pc^{-2}, and it is only 8.0×10^2 (1.7×10^3, 1.0×10^4) $M_\odot$ pc^{-2} at $[Z] = -2.0$. This naturally explains the observed dependence of the $f_\star$ suppression scale on the amplitude of the metallicity floor. It implies that the true $f_\star$ suppression realized in nature will depend on the details of the enrichment history of a given halo, which should lead to a broadening of the M_h dependence of the $f_\star$ suppression.

5. COMPARISONS WITH HIGH-REDSHIFT OBSERVATIONS

5.1. Evolution of the Luminosity Function

In Figure 18 we present a comparison of the LFs from the KT07 and KMT09 simulations and the recent high-redshift determinations from Bouwens et al. (2007, 2011) based on deep *HST* Advanced Camera for Surveys (ACS) and Wide Field Camera 3 (WFC3) observations of B ($\langle z \rangle = 3.8$), V (5.0), i (5.9), z (6.8), and Y-band (8.0) dropout galaxies. Following Bouwens et al. (2011, hereafter B10), we determine UV luminosities from the simulated SFR according to $L_{\rm UV} = 8.0 \times 10^{27}$ (SFR$/M_\odot$ yr^{-1}) erg s^{-1} Hz^{-1}, corresponding to a Salpeter initial mass function (IMF) from 0.1 to 125 $M_\odot$ and a constant SFR $\gtrsim 100$ Myr (Madau et al. 1998). We calculate SFR from our simulated galaxies by summing the mass of all young star particles with ages less than $\tau_\star = 30$ Myr and dividing by the SF timescale,

$$\rho_{\rm SFR} = \sum_{\rm age < \tau_\star} \frac{m_\star}{\tau_\star}. \qquad (11)$$

The assumption of a constant SFR over the past 100 Myr is not likely to hold for our simulated galaxies, and we therefore may be overestimating their UV luminosities by a factor of $\sim$2 or so. A Kroupa IMF, on the other hand, would result in $\sim$1.7 higher UV luminosity for a given SFR. We compare the simulated LFs to the Schechter function fits reported by B10 (as shown in solid lines), as well as to these same relations corrected for dust extinction (dashed lines) by (1.55, 0.625, 0.375, 0, 0) mag at $z = (4, 5, 6, 7, 8)$ (cf. Table 8 in B10).

The KT07 LF exceeds the uncorrected B10 LF by $\sim$1 dex at all redshifts less than 8, and over the entire range of luminosities probed by B10. Applying the B10 dust correction brings the $z = 4$ LF into agreement with the KT07 simulation. This
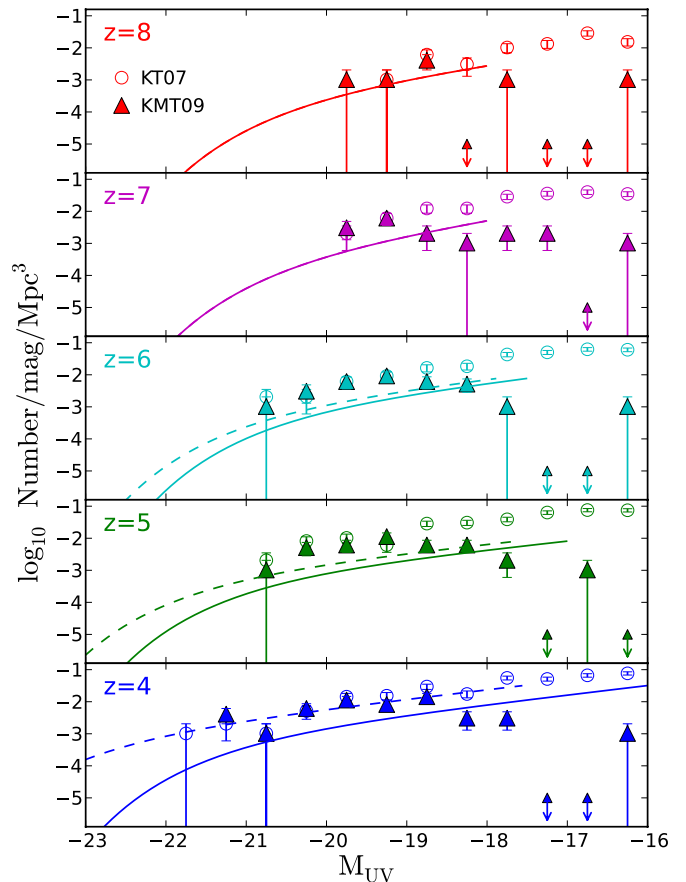

Figure 18. Luminosity function in the KT07 (open circles) and KMT09 (solid triangles) simulations compared to observational results. We calculate UV luminosities from the simulated galaxies' SFR according to $L_{\rm UV} = 8.0 \times 10^{27}$ (SFR$/M_\odot$ yr^{-1}) erg s^{-1} Hz^{-1} ($M_{\rm UV} = 51.63$–$2.5\log_{10}(L_{\rm UV}/{\rm erg\ s^{-1}\ Hz^{-1}})$), corresponding to a Salpeter IMF from 0.1 to 125 $M_\odot$ (same as Bouwens et al. 2011). Error bars are statistical only. The solid lines are the uncorrected luminosity functions reported by Bouwens et al. (2007, 2011), and the dashed lines the same relations corrected for dust extinction by (1.55, 0.625, 0.375, 0, 0) mag at $z = (4, 5, 6, 7, 8)$ (cf. Table 8 in Bouwens et al. 2011).

(A color version of this figure is available in the online journal.)

agreement is remarkable, since it results without any tuning of our models. It is puzzling, however, since it seems to imply that there is no dwarf galaxy problem at $z = 4$. In general, the steep faint-end LF slopes (-1.7 to -2.0) at $z \geqslant 4$ reported by B10 appear to be in tension with the need to strongly suppress SF efficiency in low-mass halos in order to match the lower redshift stellar mass functions and dwarf galaxy LFs. Regardless of this, at $z > 4$ the disagreement between our KT07 LFs and the dust-corrected observational ones remains substantial.

The KMT09 LF matches the KT07 one at high luminosities, reflecting the fact that H$_2$ regulation is not effective in high-mass (high-$L_{\rm UV}$) halos. Close to the sensitivity limit of the B10 observations, the KMT09 LF begins to roll over, improving the agreement between simulations and observations. This rollover, however, continues to lower luminosities, and it appears that in the KMT09 simulation the H$_2$ suppression may be too efficient at low UV luminosities, at least if the faint end of the observed UV LF continues to rise to lower luminosities. As we discussed in Section 4.2, the exact mass scale of the SF suppression (and hence the downturn of the LF) is sensitive to the nature of the metal-enrichment process and also depends on the resolution of our simulations.
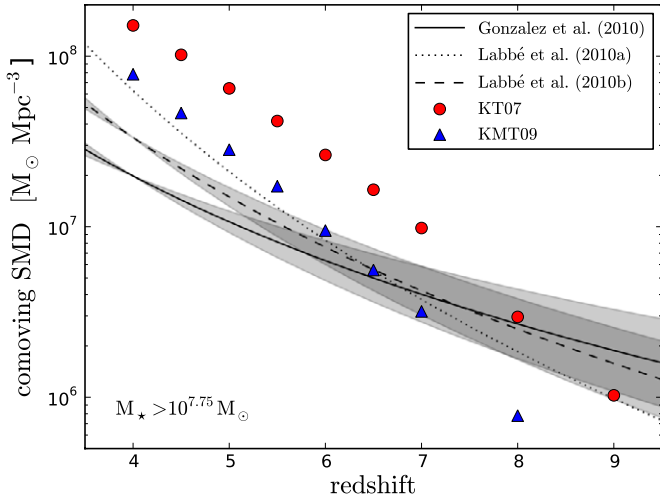
Figure 19. Stellar mass density for galaxies with $M_\star > 10^{7.75} \, M_\odot$ vs. z in the KT07 and KMT09 simulations, compared to observational determinations from González et al. (2011) (SMD $\propto (1+z)^{-3.4\pm0.8}$, solid line), Labbé et al. (2010a), (SMD $\propto (1+z)^{-6}$, dotted line), and Labbé et al. (2010b) (SMD $\propto (1+z)^{-4.4\pm0.7}$, dashed line). The uncertainty in the slope reported by González et al. (2011) and Labbé et al. (2010b) is indicated by the gray regions, arbitrarily normalized at $z = 4$.

(A color version of this figure is available in the online journal.)

5.2. Evolution of the Stellar Mass Density

In Figure 19 we show the redshift evolution of the comoving SMD contributed by galaxies with $M_\star > 10^{7.75} \, M_\odot$ in the KT07 and KMT09 simulations, compared to the observational determination from González et al. (2011). These authors used rest-frame optical photometry from *Spitzer*/IRAC to infer stellar masses for a sample of $\sim$300 $z = 4$ galaxies and combined these with *HST* ACS and WFC3/IR rest-frame UV fluxes to establish an empirical stellar mass–to–UV luminosity relation. Assuming that this same $M_\star$–$L_{\rm UV}$ extends to higher redshifts, they integrated the B10 $z = 4$–7 rest-frame UV LF down to a limiting magnitude of $M_{\rm UV} = -18$ (corresponding to $M_\star = 10^{7.75} \, M_\odot$) and obtained an empirical estimate of the SMD evolution: SMD $\propto (1+z)^{-3.4\pm0.8}$, shown as the solid line and gray region in Figure 19.

To demonstrate the systematic uncertainty in this kind of empirical determination of the stellar density evolution, we also show results from Labbé et al. (2010a) (dotted line, SMD $\propto (1+z)^{-6}$) and Labbé et al. (2010b) (dashed line, SMD $\propto (1+z)^{-4.4\pm0.7}$), who performed similar work including $z = 8$ Y-band dropouts, but used $M_\star$–$L_{\rm UV}$ relations derived from different low-redshift data (Stark et al. 2009).

Likewise, our simulated SMDs are not free from systematic uncertainties: on the one hand, they are likely somewhat underestimated, especially at high redshift, since the simulations' limited box size (12.5 Mpc) results in a delayed formation of massive halos, owing to the absence of density perturbations in the initial conditions with wavelengths exceeding the box size (Tormen & Bertschinger 1996). On the other hand, the lack of effective stellar feedback in our simulations probably artificially enhances the SMD at all redshifts.

Given the substantial uncertainties in both observations and simulations, we consider the agreement between the two to be satisfactory. We do note, however, that the simulations prefer a somewhat steeper evolution of the SMD than González et al. (2011), and that the H$_2$-regulated SF reduces the SMD by a factor of $\sim$3–5 over the covered redshift range compared to the
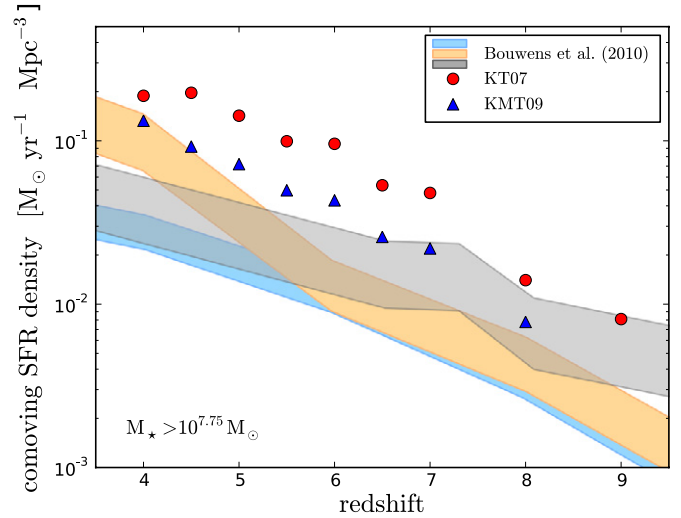

Figure 20. SFR density for galaxies with $M_\star > 10^{7.75} \, M_\odot$ vs. z in the KT07 and KMT09 simulations, compared to observational determinations from B10, which were obtained by converting rest-frame UV luminosities to SFR (Madau et al. 1998), without (blue band) and with dust corrections (orange band), and by converting stellar mass densities (Stark et al. 2009; Labbé et al. 2010a, 2010b; González et al. 2011) to SFR densities (light gray band).

(A color version of this figure is available in the online journal.)

standard SF case. The difference between KT07 and KMT09 decreases toward lower redshifts, which can be attributed to the increase of the typical halo mass (the knee in the Press–Schechter mass function) with decreasing redshift, resulting in an increasing fraction of resolved halos with mass above the $f_\star$ suppression mass scale.

5.3. Evolution of the Star Formation Rate Density

In Figure 20 we extend the comparison between our simulations and high-z observational data to the evolution of the SFR density, obtained by summing the SFR (Equation (11)) of all galaxies with $M_\star > 10^{7.75} \, M_\odot$ ($M_{\rm UV} < -18$) and dividing by the box volume. The observational data again come from B10, who derived SFR densities by converting their rest-frame UV luminosities to SFR according to Madau et al. (1998), and integrated down to a limiting magnitude of $M_{\rm UV} = -18$, with (orange band) and without (blue band) a dust correction at $z \lesssim 6$ from Bouwens et al. (2009). Note that the very blue UV continuum slopes observed in $z \gtrsim 7$ galaxies (Bouwens et al. 2010; Bunker et al. 2010; Finkelstein et al. 2010; Oesch et al. 2010) imply low dust abundances and correspondingly weak extinction corrections at these high redshifts. For comparison we also show (light gray band) the SFR density implied by the SMD evolution discussed above, assuming a fixed SMD $\propto (1+z)^{-4.4}$ extrapolation to $z \gtrsim 8$ (Labbé et al. 2010b).

Our simulated SFR densities are somewhat higher than those reported by B10. H$_2$-regulated SF, however, reduces the SFR densities by about a factor of two and brings them close to agreement with those determined from the SMD evolution, and only a factor of $\sim$3 above the luminosity-density-derived values at $z > 6$. At lower redshifts, the rise due to dust corrections in the observational SFR densities reduces the difference, and an extrapolation of the KMT09 SFR densities to $z = 4$ is in good agreement with the dust-corrected observational determination. If the observed steep UV continuum slopes are a selection effect and not representative of typical $z \gtrsim 7$ galaxies, then a more heavily dust-obscured population of galaxies that has

been missed by current surveys could close the high-redshift gap between our simulations and current data. Additionally, it is possible that a more effective stellar feedback implementation in our simulations could further reduce the simulated SFR densities.

6. SUMMARY AND DISCUSSION

Motivated by the observational fact that SF, both in the local universe (e.g., Bigiel et al. 2008) and at intermediate redshifts (e.g., Genzel et al. 2010), correlates more tightly with the density of gas in the molecular phase than the total gas density, we have implemented an H_2-regulated SF prescription in cosmological galaxy formation simulations, with the goal of investigating whether this new ingredient can help to alleviate outstanding problems in our theoretical understanding of dwarf galaxy formation.

Rather than following the non-equilibrium molecular hydrogen chemistry including time-dependent and spatially inhomogeneous radiation transfer of the ionizing and H_2-dissociating stellar radiation field (G09), we utilize in our simulations the results of 1D radiative transfer calculations of the H_2 formation–dissociation balance in an idealized spherical giant atomic–molecular complex subject to a uniform and isotropic LW radiation field (Krumholz et al. 2008, 2009; McKee & Krumholz 2010). These calculations showed that under the assumption of two-phase equilibrium in the ISM, the H_2 abundance is determined entirely by the column density and metallicity of gas on $\sim$100 pc scales—comparable to the cell size of our highest resolution grid cells.

We have deliberately chosen a weak implementation of supernova feedback in order to isolate the effects of the molecular hydrogen chemistry on SF in a cosmological setting. Remarkably, we find that accounting for the transition from H I to H_2 alone is able to fulfill one of the functions of the neglected supernova feedback, namely, the suppression of SF in low-mass halos. The main results of our study are summarized as follows:

1. Both our conventional and H_2-regulated SF prescriptions are able to reproduce the observational scaling relation between the SFR surface density and the total gas density, the KS relation (Figure 3).

2. With the conventional SF prescription the observed turnover of Σ_{SFR} at low Σ_{gas} is recovered by manually tuning an SF threshold density. The H_2-regulated prescription, however, automatically reproduces this cutoff (Figure 5) and thus reduces the number of free parameters in the SF prescription by one.

3. We are able to reproduce many of the observational results pertaining to the KS relation, for example, the slope of the molecular gas KS relation ($\Sigma_{SFR} - \Sigma_{H_2}$) and the much weaker correlation of Σ_{SFR} with the atomic gas surface density (Figure 6). We also recover the observed metallicity dependence of the low Σ_{gas} turnover in the KS relation (Figure 7), which occurs at higher Σ_{gas} in lower metallicity systems, reflecting the atomic-to-molecular gas transition. Lastly, in agreement with recent observations, we see an increased scatter in the H_2 KS relation for smaller spatial smoothing scales.

4. We expect an increased scatter in the KS relation at higher redshifts, since the typically larger stellar velocity dispersions in high-redshift systems will allow young stars to wander outside of high column density regions.

5. H_2 regulation suppresses SF in low-mass halos, reducing the need for stellar feedback (Figure 11), as previously reported by G09 and GK10 for a set of cosmological zoom-in galaxy formation simulations including non-equilibrium H_2 formation and radiative transfer. We confirm these prior results with better statistics (hundreds of halos) and without the need for a complicated and expensive radiative transfer treatment.

6. The halo mass dependence appears to be tied primarily to a difference in metal enrichment, rather than gas column density (Figure 14). On the other hand, for a given metallicity floor (set, for example, by the first generation of Population III supernovae), the star-forming ability of halos is determined by the highest column densities their gas can condense to. Low-mass halos do not have sufficiently high column density gas to allow the transition to molecular phase and hence SF.

7. Suppressing the SF efficiency in low-mass halos lowers the cosmic SMD and SFR density. We find reasonable agreement between our H_2-regulated simulation and observational determinations of the evolution of the SMD and SFR density at $z > 4$. Both simulations and observations are subject to large systematic uncertainties.

As we discussed throughout the text, a number of caveats apply to our findings. First, the results we have presented here are not completely independent of the implementation details of our simulations (e.g., two-phase equilibrium assumption, metallicity floor, numerical resolution). We therefore cannot claim with any confidence to have pinpointed the halo mass below which SF is suppressed due to the inability of gas to become molecular.

Second, given our computational resources, we were unable to continue our simulations beyond $z = 4$. It is possible that a large buildup of atomic gas will lead to a burst of SF at lower redshift ($z \simeq 1$–3), when metallicities have increased sufficiently to allow the transition to H_2 to occur, and in fact this may help to explain how the specific SFR of 10^{10}–$10^{12}\,M_{\odot}$ halos can exceed the instantaneous gas accretion rate at these redshifts (Krumholz & Dekel 2011).

Lastly, like most cosmological galaxy formation simulations to date, our simulated galaxies suffer from the so-called baryonic overcooling problem, resulting in unrealistically high central densities (and hence strongly peaked circular velocity curves) and stellar mass fractions in our high-mass halos that are too large compared to observations. Although we cannot exclude the possibility that these artificially high central densities affect the results of our study, we believe that this makes our results conservative, in the sense that a more realistic simulation with lower central gas densities would likely experience even more H_2-regulated SF suppression. Reduced central densities would demand higher metallicity for the transition to H_2 to occur, and at the same time they would allow the metals ejected by stars to become diluted more easily, thereby reducing the metallicity of the high-density star-forming gas.

Even allowing for these caveats, we believe that the atomic-to-molecular gas transition may play an important role in regulating SF in low-mass halos. It may also help to explain the result recently reported by Boylan-Kolchin et al. (2011) that collisionless simulations of galactic dark matter substructure (Via Lactea II and Aquarius) predict a number of subhalos too centrally concentrated to host any of the known Milky Way dwarf satellite galaxies. As Boylan-Kolchin et al. (2011) suggest, one possible explanation of this puzzle is that SF in

dark matter halos becomes stochastic below some mass. The sensitivity of an H_2-regulated SF prescription to early metal enrichment may provide the necessary stochasticity.

In our simulations, H_2 regulation quenches SF in dwarf galaxies at the outset, without the need to artificially enhance stellar feedback by turning off gas cooling or hydrodynamically decoupling momentum-driven winds, as is commonly done in the literature. The latter implementations of enhanced stellar feedback quench SF in dwarf galaxies due to the inability of their shallow potential wells to retain the resulting gas outflows. In H_2-regulated SF, by contrast, it is the inability of low-mass halos to accumulate a sufficiently large column density of metal-enriched material that results in suppressed SF. Efficient supernova feedback implies the presence of a large pool of hot gas and galactic winds, neither of which are necessarily present in an H_2-regulated scenario. This difference may be a good way to observationally distinguish the two mechanisms.

Taken at face value, our results imply that many low-mass dark matter halos at high redshift should be filled with relatively cold, yet atomic gas, which is prevented from becoming molecular by its low metallicity. While neutral gas surveys with radio telescopes are hard-pressed to reach beyond the local universe, constraints on the H I mass function do exist at low redshift. The ALFALFA survey (Martin et al. 2010), for example, has reported a $z \lesssim 0.06$ H I mass function down to $\log(M_{HI}/ M_\odot) = 6.2$ that is well fit by a Schechter function with a low-mass slope of $\alpha = -1.33$. This is considerably shallower than the mass function of dark matter halos ($\alpha \approx -1.8$; Boylan-Kolchin et al. 2009), indicating that not all low-mass dark matter halos can be allowed to retain their full baryonic content in the form of cold, atomic gas down to the present epoch. Another constraint may come from the statistics of DLA systems at $z \lesssim 5$ (Prochaska & Wolfe 2009; Noterdaeme et al. 2009). Whether the observed frequency distribution of DLA column densities and their covering fraction is consistent with large amounts of atomic gas in high-redshift dwarf galaxies should be investigated in detail.

Strongly suppressing SF in low-mass halos at high redshift could make it difficult for faint galaxies to reionize the universe by $z = 6$, as is commonly advocated (e.g., Madau et al. 1999). Indeed, in our simulations the total number of hydrogen ionizing photons per hydrogen atom[10] produced by $z = 6$ is reduced from ~ 18 in KT07 to ~ 6 in KMT09. As shown by Kuhlen & Faucher-Giguere (2012), a suppression scale of $M_h = 10^{10} M_\odot$ can simultaneously satisfy reionization and lower redshift Lyα forest constraints only if the escape fraction of ionizing radiation evolves strongly from $z = 4$ to higher redshifts. A slightly smaller suppression mass of $\sim 10^9 M_\odot$ (e.g., as in Krumholz & Dekel 2011), however, is in good agreement with all constraints.

While we have emphasized in this work that H_2-regulated SF can perform some of the functions typically assigned to supernova feedback, we of course acknowledge that supernovae do in fact occur in nature and that their associated injection of energy and momentum into the surrounding ISM is likely to significantly impact subsequent SF and may help to solve the problem of forming galaxies that are too concentrated in the simulations. Future research will be necessary to elucidate how

the interplay of molecular chemistry and supernova feedback shapes SF in dwarf galaxies and beyond.

APPENDIX

SOBOLEV-LIKE APPROXIMATION OF Σ

One way to alleviate the explicit resolution dependence in our implementation of the KMT09 algorithm (Equations (4)–(9)) is to use a Sobolev-like approximation of the column density (see Gnedin et al. 2009), instead of simply multiplying the grid cell density by its width. We have implemented a Sobolev-like approximation as follows:

$$\rho_x^+ = 0.5\,(\rho_{i,j,k} + \rho_{i+1,j,k}), \qquad \rho_x^- = 0.5\,(\rho_{i,j,k} + \rho_{i-1,j,k}),$$
$$h_x^+ = \frac{\rho_x^+}{|\rho_{i+1,j,k} - \rho_{i,j,k}|/\Delta x}, \qquad h_x^- = \frac{\rho_x^-}{|\rho_{i,j,k} - \rho_{i-1,j,k}|/\Delta x},$$
$$\Sigma_x^+ = \rho_x^+ \cdot h_x^+, \qquad\qquad \Sigma_x^- = \rho_x^- \cdot h_x^-, \qquad (A1)$$

and similarly for the y- and z-directions. This definition has the virtue that it is resolution-independent, at least to the extent that the density field itself is resolution-independent. To obtain a total column density, we take the harmonic mean over the six cardinal directions,

$$\langle \Sigma \rangle = \frac{6}{1/\Sigma_x^+ + 1/\Sigma_x^- + 1/\Sigma_y^+ + 1/\Sigma_y^- + 1/\Sigma_z^+ + 1/\Sigma_z^-}. \quad (A2)$$

We have applied this Sobolev-like approximation for Σ_{gas} in a post-processing analysis of the $z = 4$ output of the KMT09 simulation and compared the resulting column density with the simple grid-cell-based estimate used in the simulation; see the left panel of Figure 21. We are only showing points with $\Sigma > 50\,M_\odot$ pc^{-2}, since at lower columns the H_2 abundance, and hence SFR, is negligible. The median of Σ_{Sob} lies close to the 1–1 line but drops below it around $\Sigma_{cell} = 100\,M_\odot$ pc^{-2}, implying that the Sobolev-like approximation systematically yields slightly lower values at high Σ_{cell}. At $\Sigma_{cell} = 100$, 1000, and 5000 $M_\odot$ pc^{-2} the median of Σ_{Sob} is 101, 880, and 3930 $M_\odot$ pc^{-2}, respectively. The 1σ scatter of Σ_{Sob} around the

---

[10] We assume 4000 hydrogen ionizing photons per stellar baryon for every solar mass of stars formed, as appropriate for a Salpeter IMF from 0.1 to 125 $M_\odot$ and a mean ionizing photon energy of 20 eV (Madau et al. 1999; Leitherer et al. 1999).
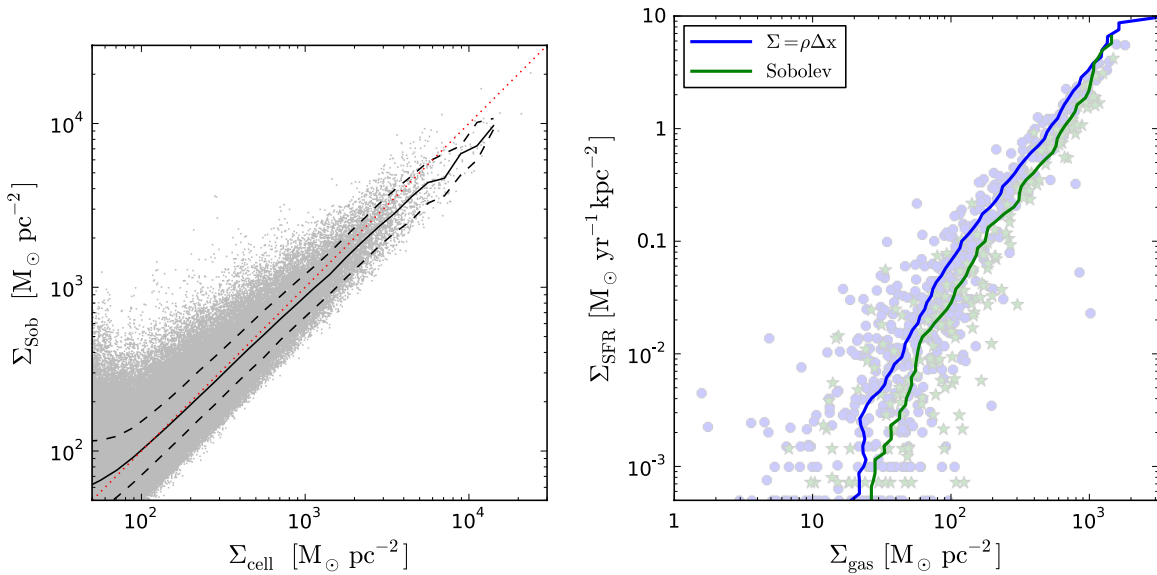
Figure 21. Left: comparison of a Sobolev-like estimate of the column density ($\Sigma_{Sob} = \rho \times (\rho/\nabla\rho)$; see the text for details) with the simple grid cell column ($\Sigma_{cell} = \rho\Delta x$), obtained by post-processing the $z = 4$ KMT09 output. Only columns greater than $50\ M_\odot$ pc^{-2} are shown, since the H$_2$ content is negligible at lower columns. The solid and dashed black lines show the median and 16th–84th percentiles of Σ_{Sob} for a given Σ_{cell}. The Sobolev-like estimate results in slightly lower columns, especially at high columns. Right: KS relation for simulation KMT09_Sob, in which the Sobolev-like approximation was used at simulation run time to calculate the column density entering the KMT09 expression for f_{H_2}. Note that we did not use the Sobolev-like approximation to determine the x-axis quantity Σ_{gas}, the column smoothed at $l = 3$ (~1 kpc). The slightly lower columns with the Sobolev-like approximation result in lower f_{H_2} and hence a slightly reduced SFR at a given Σ_{gas}.

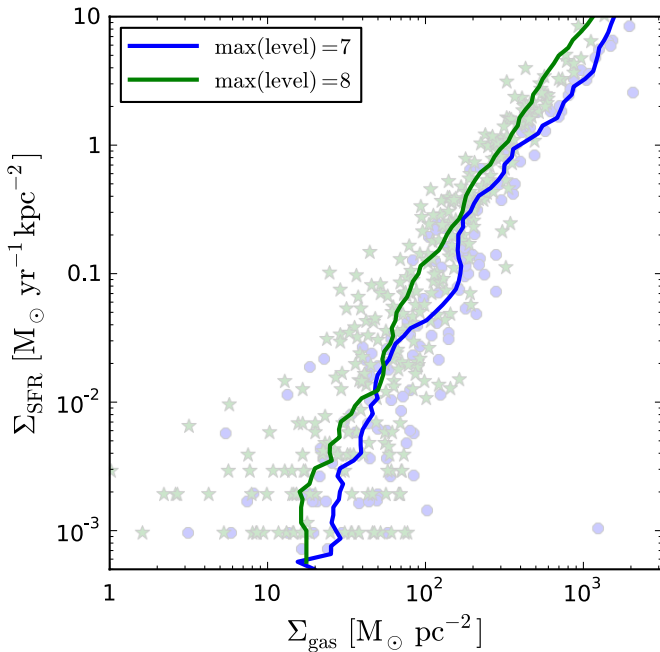(A color version of this figure is available in the online journal.)

Figure 22. Comparison of the KS relation for the KMT09_Sob and KMT09_SobL8 simulations at $z = 6$. The use of Σ_{Sob} does not fully remove the resolution dependence but reduces it mildly compared to simulations with Σ_{cell} (cf. right panel of Figure 10).

(A color version of this figure is available in the online journal.)

median is 0.26 dex (i.e., 68% of all cells lie within a factor of ~1.8 of the median).

This post-processing analysis indicates that a simulation actually using the Sobolev-like approximation at run time might have somewhat reduced SF, owing to the systematically slightly lower columns, which provide less shielding and hence

lower H$_2$ abundances. This is in fact borne out in practice, as shown in the right panel of Figure 21. We ran two additional simulations, KMT09_Sob and KMT09_SobL8, in which the column densities entering the KMT09 f_{H_2} prescription were determined at run time using the Sobolev-like estimator. Indeed, the resulting KS relation has a slightly lower normalization, indicating a somewhat reduced SF efficiency.

As discussed in the main text, to some degree there will always be a resolution dependence in the determination of the column density in our simulations, simply because we are not resolving the true Jeans length and are applying a minimum pressure support in order to prevent artificial fragmentation. This is demonstrated in Figure 22, which shows the KS relations for the KMT09_Sob and KMT09_SobL8 simulations. The corresponding plot for simulations with Σ_{cell} is the right panel of Figure 10, and a comparison between these two figures shows that the use of Σ_{Sob} only mildly reduces the resolution dependence.

The two different methods of estimating column densities (Σ_{cell}, Σ_{Sob}) are resolution dependent in different ways. The difference between the two in Σ and in the KS relation is fairly small (less than a factor of two) and does not impact the overall conclusion of our study that the metallicity-dependent nature of the atomic-to-molecular transition can play a major role in explaining the low SF efficiency in dwarf galaxies.

REFERENCES

Abel, T., Anninos, P., Zhang, Y., & Norman, M. L. 1997, New Astron., 2, 181
Agertz, O., Teyssier, R., & Moore, B. 2009, MNRAS, 397, L64
Agertz, O., Teyssier, R., & Moore, B. 2011, MNRAS, 410, 1391
Anninos, P., Zhang, Y., Abel, T., & Norman, M. L. 1997, New Astron., 2, 209
Avila-Reese, V., Colín, P., González-Samaniego, A., et al. 2011, ApJ, 736, 134
Behroozi, P. S., Conroy, C., & Wechsler, R. H. 2010, ApJ, 717, 379
Benson, A. J., Bower, R. G., Frenk, C. S., et al. 2003, ApJ, 599, 38
Benson, A. J., Frenk, C. S., Lacey, C. G., Baugh, C. M., & Cole, S. 2002, MNRAS, 333, 177

Bigiel, F., Leroy, A., Walter, F., et al. 2008, AJ, 136, 2846
Blitz, L. 1993, in Protostars and Planets III, ed. E. H. Levy & J. I. Lunine (Tucson: Univ. Arizona Press), 125
Blumenthal, G. R., Faber, S. M., Primack, J. R., & Rees, M. J. 1984, Nature, 311, 517
Bolatto, A. D., Leroy, A. K., Jameson, K., et al. 2011, ApJ, 741, 12
Bolatto, A. D., Leroy, A. K., Rosolowsky, E., Walter, F., & Blitz, L. 2008, ApJ, 686, 948
Bouwens, R. J., Illingworth, G. D., Franx, M., & Ford, H. 2007, ApJ, 670, 928
Bouwens, R. J., Illingworth, G. D., Franx, M., et al. 2009, ApJ, 705, 936
Bouwens, R. J., Illingworth, G. D., Oesch, P. A., et al. 2010, ApJ, 708, L69
Bouwens, R. J., Illingworth, G. D., Oesch, P. A., et al. 2011, ApJ, 737, 90
Boylan-Kolchin, M., Bullock, J. S., & Kaplinghat, M. 2011, MNRAS, 415, L40
Boylan-Kolchin, M., Springel, V., White, S. D. M., Jenkins, A., & Lemson, G. 2009, MNRAS, 398, 1150
Brook, C. B., Stinson, G., Gibson, B. K., Wadsley, J., & Quinn, T. 2012, MNRAS, submitted (arXiv:1201.3359)
Bryan, G. L., & Norman, M. L. 1998, ApJ, 495, 80
Bryan, G. L., Norman, M. L., Stone, J. M., Cen, R., & Ostriker, J. P. 1995, Comput. Phys. Commun., 89, 149
Bullock, J. S., Kravtsov, A. V., & Weinberg, D. H. 2000, ApJ, 539, 517
Bunker, A. J., Wilkins, S., Ellis, R. S., et al. 2010, MNRAS, 409, 855
Cen, R., & Ostriker, J. P. 1993, ApJ, 417, 404
Cen, R., & Ostriker, J. P. 2006, ApJ, 650, 560
Ceverino, D., & Klypin, A. 2009, ApJ, 695, 292
Choi, J., & Nagamine, K. 2012, MNRAS, 419, 1280
Cirasuolo, M., McLure, R. J., Dunlop, J. S., et al. 2010, MNRAS, 401, 1166
Cole, S., Lacey, C. G., Baugh, C. M., & Frenk, C. S. 2000, MNRAS, 319, 168
Colella, P., & Woodward, P. R. 1984, J. Comput. Phys., 54, 174
Colín, P., Avila-Reese, V., Vázquez-Semadeni, E., Valenzuela, O., & Ceverino, D. 2010, ApJ, 713, 535
Conroy, C., & Wechsler, R. H. 2009, ApJ, 696, 620
Cresci, G., Hicks, E. K. S., Genzel, R., et al. 2009, ApJ, 697, 115
Daddi, E., Elbaz, D., Walter, F., et al. 2010, ApJ, 714, L118
Dekel, A., & Silk, J. 1986, ApJ, 303, 39
Diemand, J., Kuhlen, M., Madau, P., et al. 2008, Nature, 454, 735
D'Onghia, E., Besla, G., Cox, T. J., & Hernquist, L. 2009, Nature, 460, 605
Draine, B. T. 1978, ApJS, 36, 595
Efstathiou, G. 1992, MNRAS, 256, 43P
Efstathiou, G. 2000, MNRAS, 317, 697
Eisenstein, D. J., & Hu, W. 1999, ApJ, 511, 5
Eisenstein, D. J., & Hut, P. 1998, ApJ, 498, 137
Fall, S. M., Krumholz, M. R., & Matzner, C. D. 2010, ApJ, 710, L142
Faucher-Giguère, C., & Kereš, D. 2011, MNRAS, 412, L118
Faucher-Giguère, C., Kereš, D., & Ma, C. 2011, MNRAS, 417, 2982
Faucher-Giguère, C., Lidz, A., Zaldarriaga, M., & Hernquist, L. 2009, ApJ, 703, 1416
Feldmann, R., & Gnedin, N. Y. 2011, ApJ, 727, L12
Feldmann, R., Gnedin, N. Y., & Kravtsov, A. V. 2011, ApJ, 732, 115
Ferland, G. J., Korista, K. T., Verner, D. A., et al. 1998, PASP, 110, 761
Finkelstein, S. L., Papovich, C., Giavalisco, M., et al. 2010, ApJ, 719, 1250
Font, A. S., Benson, A. J., Bower, R. G., et al. 2011, MNRAS, 417, 1260
Fontanot, F., Lucia, G. D., Monaco, P., Somerville, R. S., & Santini, P. 2009, MNRAS, 397, 1776
Fu, J., Guo, Q., Kauffmann, G., & Krumholz, M. R. 2010, MNRAS, 409, 515
Genel, S., Naab, T., Genzel, R., et al. 2012, ApJ, 745, 11
Genzel, R., Tacconi, L. J., Gracia-Carpio, J., et al. 2010, MNRAS, 407, 2091
Giavalisco, M., Ferguson, H. C., Koekemoer, A. M., et al. 2004, ApJ, 600, L93
Gnedin, N. Y. 1998, MNRAS, 294, 407
Gnedin, N. Y., & Kravtsov, A. V. 2010, ApJ, 714, 287
Gnedin, N. Y., & Kravtsov, A. V. 2011, ApJ, 728, 88
Gnedin, N. Y., Kravtsov, A. V., & Rudd, D. H. 2011, ApJS, 194, 46
Gnedin, N. Y., Tassis, K., & Kravtsov, A. V. 2009, ApJ, 697, 55
Gnedin, O. Y., Hernquist, L., & Ostriker, J. P. 1999, ApJ, 514, 109
Goldbaum, N. J., Krumholz, M. R., Matzner, C. D., & McKee, C. F. 2011, ApJ, 738, 101
González, V., Labbé, I., Bouwens, R. J., et al. 2011, ApJ, 735, L34
Governato, F., Brook, C., Mayer, L., et al. 2010, Nature, 463, 203
Guedes, J., Callegari, S., Madau, P., & Mayer, L. 2011, ApJ, 742, 76
Guo, Q., White, S., Li, C., & Boylan-Kolchin, M. 2010, MNRAS, 404, 1111
Haardt, F., & Madau, P. 2001, in Clusters of Galaxies and the High Redshift Universe Observed in X-Rays, ed. D. M. Neumann & J. T. T. Van (Saclay: CEA), 64
Hopkins, P. F., Quataert, E., & Murray, N. 2011, MNRAS, 417, 950
Katz, N. 1992, ApJ, 391, 502

Kauffmann, G., White, S. D. M., & Guiderdoni, B. 1993, MNRAS, 264, 201
Kennicutt, R. C. 1998, ApJ, 498, 541
Kennicutt, R. C., Calzetti, D., Walter, F., et al. 2007, ApJ, 671, 333
Klypin, A., Kravtsov, A. V., Valenzuela, O., & Prada, F. 1999, ApJ, 522, 82
Komatsu, E., Smith, K. M., Dunkley, J., et al. 2011, ApJS, 192, 18
Kravtsov, A. V. 2003, ApJ, 590, L1
Krumholz, M., & Burkert, A. 2010, ApJ, 724, 895
Krumholz, M. R., & Dekel, A. 2011, arXiv:1106.0301
Krumholz, M. R., & Gnedin, N. Y. 2011, ApJ, 729, 36
Krumholz, M. R., Leroy, A. K., & McKee, C. F. 2011, ApJ, 731, 25
Krumholz, M. R., & Matzner, C. D. 2009, ApJ, 703, 1352
Krumholz, M. R., Matzner, C. D., & McKee, C. F. 2006, ApJ, 653, 361
Krumholz, M. R., McKee, C. F., & Tumlinson, J. 2008, ApJ, 689, 865
Krumholz, M. R., McKee, C. F., & Tumlinson, J. 2009, ApJ, 693, 216
Krumholz, M. R., & Tan, J. C. 2007, ApJ, 654, 304
Kuhlen, M., & Faucher-Giguere, C. 2012, arXiv:1201.0757
Labbé, I., González, V., Bouwens, R. J., et al. 2010a, ApJ, 708, L26
Labbé, I., González, V., Bouwens, R. J., et al. 2010b, ApJ, 716, L103
Lagos, C. D. P., Lacey, C. G., Baugh, C. M., Bower, R. G., & Benson, A. J. 2011, MNRAS, 416, 1566
Larson, R. B. 1974, MNRAS, 169, 229
Leitherer, C., Schaerer, D., Goldader, J. D., et al. 1999, ApJS, 123, 3
Leroy, A. K., Walter, F., Brinks, E., et al. 2008, AJ, 136, 2782
Liu, G., Koda, J., Calzetti, D., Fukuhara, M., & Momose, R. 2011, ApJ, 735, 63
Machacek, M. E., Bryan, G. L., & Abel, T. 2001, ApJ, 548, 509
Madau, P., Diemand, J., & Kuhlen, M. 2008, ApJ, 679, 1260
Madau, P., Haardt, F., & Rees, M. J. 1999, ApJ, 514, 648
Madau, P., Pozzetti, L., & Dickinson, M. 1998, ApJ, 498, 106
Marchesini, D., van Dokkum, P. G., Schreiber, N. M. F., et al. 2009, ApJ, 701, 1765
Martin, A. M., Papastergis, E., Giovanelli, R., et al. 2010, ApJ, 723, 1359
Matzner, C. D. 2002, ApJ, 566, 302
Mayer, L., Mastropietro, C., Wadsley, J., Stadel, J., & Moore, B. 2006, MNRAS, 369, 1021
McKee, C. F. 1989, ApJ, 345, 782
McKee, C. F., & Krumholz, M. R. 2010, ApJ, 709, 308
Moore, B., Ghigna, S., Governato, F., et al. 1999, ApJ, 524, L19
Moster, B. P., Somerville, R. S., Maulbetsch, C., et al. 2010, ApJ, 710, 903
Murray, N., Quataert, E., & Thompson, T. A. 2010, ApJ, 709, 191
Nagamine, K., Ostriker, J. P., Fukugita, M., & Cen, R. 2006, ApJ, 653, 881
Nakamura, F., & Li, Z. 2007, ApJ, 662, 395
Norman, C., & Silk, J. 1980, ApJ, 238, 158
Noterdaeme, P., Petitjean, P., Ledoux, C., & Srianand, R. 2009, A&A, 505, 1087
Ocvirk, P., Pichon, C., & Teyssier, R. 2008, MNRAS, 390, 1326
Oesch, P. A., Bouwens, R. J., Illingworth, G. D., et al. 2010, ApJ, 709, L16
Oppenheimer, B. D., & Davé, R. 2006, MNRAS, 373, 1265
Oppenheimer, B. D., Davé, R., Kereš, D., et al. 2010, MNRAS, 406, 2325
O'Shea, B. W., Nagamine, K., Springel, V., Hernquist, L., & Norman, M. L. 2005, ApJS, 160, 1
Piontek, F., & Steinmetz, M. 2011, MNRAS, 410, 2625
Prochaska, J. X., & Wolfe, A. M. 2009, ApJ, 696, 1543
Rafelski, M., Wolfe, A. M., & Chen, H. 2011, ApJ, 736, 48
Rafelski, M., Wolfe, A. M., Cooke, J., et al. 2009, ApJ, 703, 2033
Rashkov, V., Madau, P., Kuhlen, M., & Diemand, J. 2012, ApJ, 745, 142
Robertson, B. E., & Kravtsov, A. V. 2008, ApJ, 680, 1083
Rodríguez, M., & Delgado-Inglada, G. 2011, ApJ, 733, L50
Sales, L. V., Navarro, J. F., Schaye, J., et al. 2010, MNRAS, 409, 1541
Schaye, J., Dalla Vecchia, C., Booth, C. M., et al. 2010, MNRAS, 402, 1536
Schruba, A., Leroy, A. K., Walter, F., Sandstrom, K., & Rosolowsky, E. 2010, ApJ, 722, 1699
Sheth, R. K., & Tormen, G. 1999, MNRAS, 308, 119
Smith, B., Sigurdsson, S., & Abel, T. 2008, MNRAS, 385, 1443
Smith, B. D., Hallman, E. J., Shull, J. M., & O'Shea, B. W. 2011, ApJ, 731, 6
Somerville, R. S., Hopkins, P. F., Cox, T. J., Robertson, B. E., & Hernquist, L. 2008, MNRAS, 391, 481
Springel, V., Frenk, C. S., & White, S. D. M. 2006, Nature, 440, 1137
Springel, V., & Hernquist, L. 2003, MNRAS, 339, 289
Springel, V., Wang, J., Vogelsberger, M., et al. 2008, MNRAS, 391, 1685
Stadel, J., Potter, D., Moore, B., et al. 2009, MNRAS, 398, L21
Stark, D. P., Ellis, R. S., Bunker, A., et al. 2009, ApJ, 697, 1493
Stinson, G., Seth, A., Katz, N., et al. 2006, MNRAS, 373, 1074
Thacker, R. J., & Couchman, H. M. P. 2000, ApJ, 545, 728
Tormen, G., & Bertschinger, E. 1996, ApJ, 472, 14
Toro, E. F., Spruce, M., & Speares, W. 1994, Shock Waves, 4, 25

Turk, M. J., Smith, B. D., Oishi, J. S., et al. 2011, ApJS, 192, 9
Wang, J., Lucia, G. D., Kitzbichler, M. G., & White, S. D. M. 2008, MNRAS, 384, 1301
Wang, P., Li, Z., Abel, T., & Nakamura, F. 2010, ApJ, 709, 27
White, S. D. M., & Rees, M. J. 1978, MNRAS, 183, 341
Wise, J. H., Turk, M. J., Norman, M. L., & Abel, T. 2012, ApJ, 745, 50
Wolfe, A. M., & Chen, H. 2006, ApJ, 652, 981

Wolfire, M. G., McKee, C. F., Hollenbach, D., & Tielens, A. G. G. M. 2003, ApJ, 587, 278
Wolfire, M. G., Tielens, A. G. G. M., Hollenbach, D., & Kaufman, M. J. 2008, ApJ, 680, 384
Wong, T., & Blitz, L. 2002, ApJ, 569, 157
Yepes, G., Kates, R., Khokhlov, A., & Klypin, A. 1997, MNRAS, 284, 235
Zheng, Z., Coil, A. L., & Zehavi, I. 2007, ApJ, 667, 760